Supplementary Information for

Intensified subduction carbon cycling drove early Earth climate change and oxygenation

Xiao Wang[1], Wen-Yong Duan[2, 3*], Taras Gerya[2], James A.D. Connolly[2], Benjamin J. W. Mills[4], Sanzhong Li[3], Yu-Fei Xuan[5], Xiao-Xi Zhu[1], Jian Zhang[1*]

[1] *NWU-HKU Joint Centre of Earth and Planetary Sciences, Department of Earth and planetary Sciences, The University of Hong Kong, Pokfulam Road, Hong Kong*

[2] *Department of Earth Sciences, Swiss Federal Institute of Technology, Zurich 8092, Switzerland*

[3] *Frontiers Science Center for Deep Ocean Multispheres and Earth System, Key Lab of Submarine Geosciences and Prospecting Techniques, MOE and College of Marine Geosciences, Ocean University of China, Qingdao 266100, China*

[4] *School of Earth and Environment, University of Leeds, Leeds LS29JT, United Kingdom*

[5] *Guangzhou Marine Geological Survey, China Geological Survey, Guangzhou, 511458，China*

[*] ***Corresponding author: Wen-Yong Duan (wenyong.duan@eaps.ethz.ch), Jian Zhang (jian@hku.hk)***

This file includes:

Supplementary Text S1

1. Geological background

The North China Craton (NCC), comprising Archean basement terranes of both the Eastern and Western Blocks, achieved its final amalgamation during the Paleoproterozoic through the Trans-North China Orogeny[1]. The Yinshan Block, a typical Neoarchean Block of the NCC, consists of the Guyang granite-greenstone belt and the Wuchuan high-grade complex (Text S1-Fig. 1). The lower unit of Neoarchean greenstone sequences from Guyang granite-greenstone belt is composed mainly of ultramafic rocks (komatiite) and mafic volcanic rocks[2-3]. The mafic granulites from Wuchuan complex are represented by garnet two-pyroxene granulite and hornblende two-pyroxene granulite[4-6]. All of them were emplaced in the late Neoarchean (2.6–2.5 Ga), with most forming between 2.55 and 2.50 Ga[7].

2. Results

2.1 Zircon U-Pb dating

In this study, we selected six Neoarchean basalt samples from Guyang and Wuchuan area for zircon U–Pb dating. Zircon grains from these samples exhibit stubby to prismatic shapes. Their oscillatory zoning morphology is a characteristic of zircons originating from magmas. Sample 21GY63-4 yield weighted mean $^{207}Pb/^{206}Pb$ age of 2567 ± 11 Ma (n = 37; MSWD = 0.037); Sample 21GY64-1 yield weighted mean $^{207}Pb/^{206}Pb$ age of 2535 ± 11 Ma (n = 40; MSWD = 0.0079); Sample 21GY32-1 yield weighted mean $^{207}Pb/^{206}Pb$ age of 2530 ± 12 Ma (n = 36; MSWD = 0.032); Sample 21GY48-2 yield weighted mean $^{207}Pb/^{206}Pb$ age of 2533 ± 10 Ma (n = 44; MSWD = 0.014); Sample 21GY50-3 yield weighted mean $^{207}Pb/^{206}Pb$ age of 2520 ± 14 Ma (n = 24; MSWD = 0.027); Sample 19WC11-8 yield weighted mean $^{207}Pb/^{206}Pb$ age of 2495 ± 22 Ma (n = 28; MSWD = 2.0). Thus, Magmatic zircons from the studied samples yield $^{207}Pb/^{206}Pb$ ages ranging from 2567 to 2495 Ma (Text S1-Fig. 2), interpreted as the crystallization age of the studied Neoarchean basalts.

2.2 Major and trace element geochemistry

Fifty-four Neoarchean basalts were analyzed for whole-rock major and trace elements, with the analytical data presented in Table S1. These samples exhibit the following major oxide compositions (wt.%): SiO_2 (45.18–51.90), Na_2O (1.67–4.15), K_2O (0.33–2.99), Al_2O_3 (9.83–18.47), TFe_2O_3 (9.87–18.15) and MgO (3.48–12.49). The Mg# ($Mg^{2+}/(Mg^{2+}+TFe^{2+})$ molar ratio values for these samples range from 29 to 71. The studied basaltic rocks include basalt, basaltic andesite, and andesite (Text S1-Fig. 3A), exhibit a trend from the low-K calc-alkaline series toward the shoshonitic series (Text S1-Fig. 3B). The samples have low $(La/Yb)_N$ ratios of 2.0–22.4. They exhibit depletions in high field strength elements (HFSEs) such as Nb, Ta, P and Ti, along with relative enrichments in large-ion lithophile elements (LILEs) such as Rb, Ba and Pb (Text S1-Figs. 3C, D), indicating a typical arc magmatic affinity[8].

2.3 Whole rock Sr-Nd isotope compositions

Twenty-five samples selected for Sr-Nd isotopic analysis, Table S2 present the whole-rock Sr-Nd isotope analyses for the Neoarchean basalts from Guyang and Wuchuan area. The initial $(^{87}Sr/^{86}Sr)_i$ ratios of Neoarchean basalts range from 0.694695 to 0.706571, and the negative to positive $\varepsilon_{Nd}(t)$ values range from -2.41 to +6.84 with a mean T_{DM1} age of 2.75 Ga.

3. Effects of shallow-level magma processes

First of all, all studied samples display coherent patterns on chondrite-normalized and primitive mantle-normalized diagrams (Text S1-Figs. 3C, D), which are inconsistent with significant post-magmatic alteration. Secondly, these samples exhibit low LOI contents (-0.16–3.35 wt. %) and no obvious Ce anomalies (δCe = 0.88–1.10). Besides, the lack of correlations between δ^7Li or $\delta^{26}Mg$ and LOI values indicates the Li–Mg isotopic systems have not been affected by post-magmatic alteration (Text S1-Figs. 4A, B).

Mantle-derived magma inevitably undergoes contamination by shallow crustal materials during magma ascent, due to its high temperature and low viscosity[9]. Crustal contamination elevates incompatible element abundances (e.g., Th, Zr, Hf) in the mafic magmas. However, these basalts display Th/Ce values (0.003–0.11; mean =0.04) and Th/La values (0.01–0.21; mean =0.09), which

are lower than those of continental crust[10] (Th/Ce =0.15; Th/La =0.27). In addition, significant crustal contamination may elevate LREE/HREE ratios[11], while these studied Neoarchean basalts exhibit low LREE/HREE ratios (2.80–14.15). Moreover, such slightly negative to positive zircon $\varepsilon_{Nd}(t)$ (-2.41–+6.84) of our studied samples cannot result from great contributions of old crustal materials. The lack of correlations between whole-rock SiO_2 contents and Th/La ratios, and whole-rock MgO contents and Nb/La ratios (Text S1-Figs. 4C, D), indicate that the influence of crustal contamination was negligible. More importantly, mafic magmas affected by crustal contamination exhibit low Nb/Ta[12]. Thus, the insignificant correlations between δ^7Li or δ^{26}Mg and Nb/Ta ratios indicate a limited contamination. (Text S1-Figs. 4E, F).

Under the high-temperature conditions typical of the mantle, such as those involved in magmatic activities, the isotopic fractionation factors for Li isotopes tend to approach unity[13]. The lack of correlation of the δ^7Li values with SiO_2 contents (Text S1-Fig. 5A), also demonstrated that the Li isotopic system of the studied samples was not notably influenced by fractional crystallization[14]. Previous studies by Teng et al. (ref. [15]) have shown that during the high-temperature differentiation of mafic magma, the fractional crystallization of olivine and pyroxene produces only limited Mg isotopic fractionation ($\Delta\delta^{26}$Mg < 0.07‰). Moreover, there is no obvious correlation between δ^{26}Mg values with SiO_2 or MgO contents (Text S1-Fig. 5B), further indicating that fractional crystallization of silicate phases (e.g., olivine) cannot account for the Mg isotopic anomalies. Fractional crystallization of chromite and Fe-Ti oxides is known to result in decreased δ^{26}Mg values[16]. However, our samples show no correlations between δ^{26}Mg and TFe_2O_3, nor between δ^{26}Mg and Cr contents (Text S1-Figs. 5C, D), indicating that the fractional crystallization of these minerals (Fe-Ti oxides and chromite) did not drive the observed variations in Mg isotopes.

These studied samples are likely products of partial melting, as suggested by their strong linearity in the Ce/Zr vs. Ce and La/Hf vs. La diagrams (Text S1-Figs. 6A, B). Notably, Mg isotopic variations in mantle-derived magmas are influenced by the extent of partial melting, with low-degree partial melting tending to lighter δ^{26}Mg values[17-18]. The La/Yb, La/Hf and Nb/Zr ratios serve as indicators of partial melting[19]. The lack of linear correlation of the δ^{26}Mg values with La/Yb, La/Hf and Nb/Zr ratios demonstrated that the variations in Mg isotopes of the studied samples was

not notably influenced by partial melting (Text S1-Figs. 6C, D, E, F). Furthermore, Teng et al. (ref. [20]) has demonstrated that the equilibrium Mg isotopic fractionation at magmatic temperatures is insignificant during metamorphic dehydration, partial melting, and fractional crystallization.

Therefore, the whole-rock major and trace element compositions and the Li-Mg isotopic compositions of this study represent characteristics of their mantle source.

4. Magma source

The studied basalts have low La/Nb (mean = 3.23) and La/Ta (mean = 61.21) ratios, which are consistent with the high La/Nb (>1) and La/Ta (>20) ratios of basalts with a lithospheric mantle origin. In the Nb/La versus La/Yb diagram[21] (Text S1-Fig. 7A), the samples also fall within the field of the lithospheric mantle. The studied samples have more positive $\varepsilon_{Nd}(t)$ (mean = +2.17) values, indicating the parental magmas from the depleted lithospheric mantle (Text S1-Fig. 7B). Although the upper mantle is predominantly composed of peridotite[22], pyroxenite is also recognized as an important lithological component[23]. Certain geochemical indicators—such as FC3MS ($FeO^T/CaO-3\times MgO/SiO_2$)—as well as specific oxide element contents, can be used to constrain mantle source lithology[22]. The studied basalts exhibit high FC3MS values, indicating a pyroxenite-derived melt (Text S1-Fig. 7C). In the La/Sm versus La/Yb diagram (Text S1-Fig. 7D), these samples could be generated from 1–10% partial melting of spinel-garnet pyroxenite. Moreover, compared to Nb, Th and Ce, the more mobile elements (La, Ba and Pb) are preferentially extracted by slab-derived fluids during subduction. The residual oceanic crust was depleted in these elements, with higher Ce/Pb and Nb/La ratios and lower Ba/Th ratios in the subducted slab[24-25]. The studied basalts display lower Ce/Pb (1.1–20.8) and Nb/La (0.10–0.39) ratios and higher Ba/Th (25.5–3575.6; mean = 675.0) than those ratios for AOC[26] (Ce/Pb = 65.4; Nb/La = 1.16; Ba/Th = 74.9), indicating that AOC played a restricted role in the source composition.

Based on light $\delta^{26}Mg$ and heavy $\delta^{7}Li$ isotopic signatures, we propose that the Neoarchean basalts were derived from a heterogeneous mantle source, such as carbonate-metasomatism mantle sources. Whether formed as biogenic seawater precipitates or non-biogenic products of seawater-rock interaction, these carbonates share a common geochemical signature: marked enrichments in

P, Sr, and LREE (relative to HREE), coupled with depletions in HFSE[27-29]. The studied basalts have higher abundances of P_2O_5 (0.07–1.39 wt.%; mean = 0.43 wt.%), Sr (121–1866 ppm; mean = 640 ppm). They also have higher Eu/Ti and lower Hf/Hf* and Ti/Ti* ratios (Extended Data Fig. 1). These characteristics point to the derivation of Neoarchean basalts from a mantle source containing carbonate components. Carbonate reaches subduction zones through two primary reservoirs including sediments and AOC [29, 30-32]. Prior studies suggested that subducted sediments enriched Nb, Ta, Th and U, generating higher Th/Yb and lower Ba/La ratios than slab components[18, 33]. The studied basalts have higher δ^7Li values with lower Ba/La ratios and lower δ^{26}Mg values with higher Th/Yb ratios (Extended Data Figs. 2A, B), indicating dominant carbonate-bearing sediment contributions to the mantle source.

In this study, samples with lower Ce/Pb and Nb/U ratios than MORB and OIB, have higher Th/Yb ratios, indicating an enriched metasomatism (Text S1-Figs. 8A, B). In general, metasomatism in subduction zones operates through two main types: hydrous melts and slab-derived fluids. The concentrations of incompatible elements in arc magmas reflect metasomatic processes mediated by slab-derived fluids. During subduction, LILEs (Rb, Ba, Sr, U, Pb) are mobilized by slab-derived fluids, whereas Th and LREEs remain sequestered in the oceanic crust unless transported via slab melts or sediment-derived melts into the mantle wedge[34]. Magmas derived from a sub-continental lithospheric mantle source modified by fluids exhibit higher Ba/Nb, La/Nb, and Ba/Zr ratios but lower Nb/Th ratios than those influenced by melts. The high Ba/Nb and Ba/Zr ratios (mean = 88.64 and 7.91, respectively) and low Nb/Th ratios (mean = 7.41) of the studied rocks are indicative of fluid metasomatism. Moreover, the correlations between δ^{26}Mg and Ba/Th, Nb/Yb and Ba/Nb, Sr/Y and Nb/Y, Ba/Th and Th/La collectively highlight the significant fluids contribution to the lithospheric mantle source during Neoarchean (Text S1-Figs. 8C, D, E, F).

Supplementary Text S2 Details of the analytical methods

1. Whole-rock major- and trace element

The present study utilizes robust analytical protocols for whole-rock geochemical analysis. Major oxide concentrations were measured by wavelength-dispersive X-ray fluorescence (WD-XRF) spectrometry on a Rigaku ZSX Primus II instrument hosted at Wuhan SampleSolution Analytical Technology Co., Ltd., Wuhan, China. The instrument operates with a 4.0 kW Rh-target X-ray tube under fixed conditions of 50 kV acceleration voltage and 60 mA current, utilizing Kα emission lines for all target elements. Data matrix corrections were applied based on the theoretical alpha coefficient method, achieving analytical precision with a relative standard deviation (RSD) better than 2%.

Trace element abundances were quantitated using an Agilent 7700e inductively coupled plasma mass spectrometer (ICP–MS) with an accuracy better than 10%. To minimize matrix effects and ensure complete digestion of silicate minerals, powdered samples were subjected to a two-step high-pressure digestion scheme. The detailed sample-digesting procedure was as follows: (1) Sample powder (200 mesh) were placed in an oven at 105 ℃ for drying of 12 hours; (2) 50 mg sample powder was accurately weighed and placed in a Teflon bomb; (3) 1 ml HNO_3 and 1 ml HF were slowly added into the Teflon bomb; (4) Teflon bomb was putted in a stainless steel pressure jacket and heated to 190 ℃ in an oven for >24 hours; (5) After cooling, the Teflon bomb was opened and placed on a hotplate at 140 ℃ and evaporated to incipient dryness, and then 1 ml HNO_3 was added and evaporated to dryness again; (6) 1 ml of HNO_3, 1 ml of MQ water and 1 ml internal standard solution of 1 ppm In were added, and the Teflon bomb was resealed and placed in the oven at 190 ℃ for >12 hours; (7) The final solution was transferred to a polyethylene bottle and diluted to 100 g by the addition of 2% HNO_3.

2. Whole-rock Sr–Nd isotopes

Whole-rock Sr–Nd isotope analyses were conducted at the Wuhan SampleSolution Analytical Technology Co., Ltd., Wuhan, China. Prior to instrumental analysis, samples underwent rigorous

chemical processing within a class 1000 positive-pressure clean laboratory, utilizing class 100 laminar flow workbenches to mitigate contamination. The digestion procedure involved spiking approximately 50–200 mg of pre-dried (105 ℃, 12 h) 200-mesh sample powder with concentrated 1–3 ml HNO_3 and 1–3 ml HF in the Teflon bomb. These vessels were enclosed within stainless steel jackets and heated at 190 ℃ for over 24 hours to ensure complete dissolution. Post-digestion, solutions were successively evaporated to incipient dryness on a hotplate (140 ℃), followed by a final treatment with suprapure HNO_3. The residue was taken up in 1.0 mL of 2.5 M HCl. Subsequently, Sr and Nd were isolated via cation-exchange column chromatography using AG50W resin. After loading the sample, matrix elements were effectively removed by washing with 20 mL of 2.5 M HCl. Target elements were selectively eluted with stepwise additions of distinct hydrochloric acid concentrations—10 mL of 2.5 M HCl for Sr and 5 mL of 0.3 M HCl for Nd—and gently evaporated to dryness ready for mass spectrometric measurement.

Sr–Nd isotope analyses were performed on a Neptune Plus MC–ICP–MS (Thermo Fisher Scientific, Dreieich, Germany). The Neptune Plus, a double focusing MC–ICP–MS, was equipped with seven fixed electron multiplier ICs, and nine Faraday cups fitted with 10^{11} Ω resistors. The faraday collector configuration of the mass system was composed of an array from L4 to H3 to monitor $^{83}Kr^{+}$, $^{167}Er^{++}$, $^{84}Sr^{+}$, $^{85}Rb^{+}$, $^{86}Sr+$, $^{173}Yb^{++}$, $^{87}Sr^{+}$, $^{88}Sr^{+}$, $^{142}Nd^{+}$, $^{143}Nd^{+}$, $^{144}Nd^{+}$, $^{145}Nd^{+}$, $^{146}Nd^{+}$, $^{147}Sm^{+}$, $^{148}Nd^{+}$, $^{149}Sm^{+}$, $^{150}Nd+$. The large dry interface pump (120 m^3 hr^{-1} pumping speed), the newly designed H and X skimmer cone and the standard sample cone were used to increase the instrumental sensitivity. Sr–Nd single element solutions from Alfa (Alfa Aesar, Karlsruhe, Germany) were used to optimize instrument operating parameters.

The exponential law, which was initially developed for TIMS measurement[35] and remains the most widely accepted and utilized with MC–ICP–MS, was used to assess the instrumental mass discrimination in this study. Mass discrimination correction was carried out via internal normalization to a $^{88}Sr/^{86}Sr$ ratio of 8.375209 and a $^{146}Nd/^{144}Nd$ ratio of 0.7219[36]. International standards of NBS987and GSB were used as bracketing standards to monitor the instrument drift during the analysis of Sr and Nd. Repeated analysis for NBS987 gives an average $^{87}Sr/^{86}Sr$ = 0.710241 ± 12 (2σ). Repeated analysis for GSB gives an average $^{143}Nd/^{144}Nd$ = 0.512439 ± 1 (2σ).

All data reduction for the MC–ICP–MS analysis of Sr–Nd isotope ratios was conducted using "Iso-Compass" software[37].

3. Whole-rock Li isotopes

Whole-rock Li isotopic analyses were conducted at the Wuhan SampleSolution Analytical Technology Co., Ltd, Hubei, China. All operations were performed on certified Class 100 laminar flow benches situated within a positively pressurized Class 1000 clean laboratory to prevent spectral interference from atmospheric particulates. For silicate-rich samples, approximately 50–100 mg of finely ground powder was placed into a custom-made, high-pressure digestion vessel lined with PTFE. Digestion commenced with the slow addition of a 1:1 v/v mixture of concentrated nitric and hydrofluoric acids. This sealed assembly was heated at 190 ℃ for 48 hours to ensure complete dissolution of refractory phases. Upon cooling, the vessel contents were evaporated to dryness. Two successive treatments with concentrated HNO_3, each followed by evaporation, were carried out to drive off residual fluorides. To achieve a clear solution amenable to ion exchange, the residue was treated with 1 mL of HNO_3 and 2 mL of high-purity water, heated at 190 ℃ for 12 hours, and subsequently converted to the chloride form. The final residue was dissolved in 0.28 mol/L HCl, creating the load solution for column chemistry.

The separation of Li isotopes was achieved using AG 50W-X8 cation exchange resin produced by Bio-Rad [38]. After loading the sample solution into a pre-cleaned cation exchange column, matrix elements were eluted using 24 mL of 0.28 mol/L HCl, followed by a further rinse with 31 mL of 0.28 mol/L HCl to collect Li. Prior to analysis, the collected Li fraction was evaporated to dryness and converted to nitrate species.

Li isotopes analyses were performed on a Neptune Plus MC–ICP–MS (Thermo Fisher Scientific, Dreieich, Germany). Static collection mode was employed to simultaneously collect ^{7}Li and ^{6}Li by optimizing the zoom and dispersion parameters. Samples were introduced at a concentration of 50 ppb in 2% HNO_3 and a flow rate of 50 μL min^{-1}, yielding a sensitivity of ~2 V for $^{7}Li^{+}$. Instrument fractionation was corrected using the sample-standard bracketing (SSB) method. All Li isotope data were reported as per mil deviations relative to the reference material (RM) L-

SVEC:

$$\delta^7Li\ (‰) = [(^7Li/^6Li)_{sample}/(^7Li/^6Li)_{L\text{-}SVEC} - 1] \times 1000$$

Instrument performance and procedural accuracy were monitored by analyzing at least two international geological reference materials (e.g., BCR-2, RGM-2, GSP-2) with each analytical batch. The long-term external reproducibility of δ^7Li values for these standards is consistently better than ±0.40‰, confirming the high precision and accuracy of the method.

4. Whole-rock Mg isotopes

Whole-rock Mg isotopic analyses were conducted at the Wuhan SampleSolution Analytical Technology Co., Ltd, Hubei, China. All chemical processing occurred on Class 100 laminar flow benches situated within a positively pressurized Class 1000 clean room, effectively minimizing exposure to ambient contaminants to maintain analytical integrity. All chemical preparations were performed on class 100 work benches within a class 1000 overpressured clean laboratory. The detailed operation process is listed as following. Based on the MgO content of the sample, a portion of each sample powder containing 20 μg of Mg was weighed into Teflon bombs. Then, 2ml HNO_3–HF mixed acid (1:1, v/v) was added, and the sealed bomb was placed in an electric oven at 190 ℃ for 48 hours to digest the sample. After cooling, the bomb was opened and placed on a hotplate to evaporated to dryness. This was followed by adding 1 ml HNO_3 and evaporating to dryness. This step was repeated twice to completely remove fluoride. After that, the residue was re-dissolved by adding 1 ml of HNO_3 and 2 ml of ultra-pure water. The bomb was resealed and placed in an electric oven at 190℃ for 12 hours to obtain a clear digestion solution. The final solution was evaporated and re-dissolved in 200 μl 1.5N HNO_3 for chemical separation.

The chemical isolation of magnesium followed a refined three-column procedure as described by Wang et al. (ref. [39]). Step one: The digested sample was loaded into a column filled with AG50W-X8 resin (200~400 mesh), and subsequently rinsed with 20 ml of 1.5N HNO_3. All fractions from both loading and rinsing were collected for the quantitative recovery of Mg. The residual matrix elements (such as Al, Fe, Ca) are then eluted from the resin using 6N HCl. Step two: The Mg solution obtained in step one was evaporated and loaded to the same column which was pre-cleared. Matrix

elements are washed with 1N HNO_3, and the Mg fraction was collected through the elution with 17 ml 1N HNO_3. Step three: Repeat step two to further improve the purity of the Mg solution. After the three-column chemical purification process, all the interference elements were effectively separated from Mg. The recovery of Mg obtained was 100% ± 3%, and the total blank of the entire process was less than 12 ng.

Mg isotopic measurement was performed on a Thermo Fisher Scientific Neptune Plus MC–ICP–MS at Wuhan SampleSolution Analytical Technology Co., Ltd. Operated in low-resolution mode, samples were introduced via a desolvating nebulizer at a concentration of 200 ppb Mg in 2% (m/m) HNO_3. To correct for instrumental mass fractionation, the sample-standard bracketing (SSB) technique was employed. All raw isotope ratios were first normalized against the Chinese national standard, GSB Mg. These values were then converted to the widely used DSM3 reference frame based on the inter-calibration relationship established by Bao et al. (ref. [40]). The converted formula is as follows:

$$\delta^{26,25}\mathrm{Mg}\ (‰) = [(^{26,25}\mathrm{Mg}/^{24}\mathrm{Mg})_{\mathrm{sample}}/(^{26,25}\mathrm{Mg}/^{24}\mathrm{Mg})_{\mathrm{GSB\ Mg}} - 1] \times 1000;$$

$$\delta^{26/24}\mathrm{Mg}_{\mathrm{DSM3}} = \delta^{26/24}\mathrm{Mg}_{\mathrm{sample\ -\ GSB\ Mg}} - 2.05;$$

$$\delta^{25/24}\mathrm{Mg}_{\mathrm{DSM3}} = \delta^{25/24}\mathrm{Mg}_{\mathrm{sample\ -\ GSB\ Mg}} - 1.06.$$

Each batch of samples includes at least two international geological reference standards to monitor the performance of instrumental measurement and chemical separation, ensuring the accuracy and precision of the results. Repeated measurements of the geological standards (e.g., BCR-2, GSR-1 and GSP-2) in the laboratory were consistent with previously reported data, and the long-term reproducibility of δ^{26}Mg was better than 0.06‰.

5. Details of the analytical methods

We conducted quantitative source-mixing modeling for the whole-rock Mg–Sr isotopic compositions of the studied mafic rocks to quantify the proportions of recycled crustal components [41]. The equation of the above modeling is expressed by:

$$I_n = \frac{I_a \times C_a - I_a \times C_a \times N + I_b \times C_b \times N}{C_a - C_a \times N + C_b \times N}$$

Where C_a, and C_b, are the concentrations of an element in endmember a, and in endmember b, respectively. N (0−100%) is the degree of mixing. I_a, and I_b are the isotopic ratios of an element in endmember a, and in endmember b, respectively. Lowercase letters, a, and b, represent two endmembers, and n is a mixed endmember resulted from mixing of endmembers a and b.

Supplementary Text S3 Figure 1 References

The cited Phanerozoic Li isotopic compositions of Mid-ocean ridge basalt (MORB) from Tomascak et al. (ref. [1]), Marschall et al. (ref. [2]); Ocean island basalt (OIB) from Ryan et al. (ref. [3]), Krienitz et al. (ref. [4]); Arc lava from Tang et al. (ref. [5]), Hanna et al. (ref. [6]), Liu et al. (ref. [7]); Silicate sediment from Bouman et al. (ref. [8]), Tang et al. (ref. [5]), Brens et al. (ref. [9]); Carbonate sediment from Lechler et al. (ref. [10]), Sun et al. (ref. [11]), Murphy et al. (ref. [12]), Wei et al. (ref. [13]); Dehydrated oceanic crust from Marschall et al. (ref. [14]). The cited Phanerozoic Mg isotopic compositions of MORB from Wiechert and Halliday (ref. [15]), Bourdon et al. (ref. [16]), Teng et al. (ref. [17]), Hong et al. (ref. [18]); OIB from Bourdon et al. (ref. [16]), Teng et al. (ref. [16]), Zhong et al. (ref. [19]), Wang et al. (ref. [20]); Arc lava from Teng et al. (ref. [21]); Li et al. (ref. [22]), Brewer et al. (ref. [23]), Ding et al. (ref. [24]), Yuan et al., ref. [25]); Silicate sediment from Li et al. (ref. [26]); Huang et al. (ref. [27]), Qu et al. (ref. [28]); Carbonate sediment from Geske et al. (ref. [29]), Fantle and Higgins (ref. [30]); Kasemann et al. (ref. [31]); Liu et al. (ref. [32]); Higgins and Schrag (ref. [33]); Peng et al. (ref. [34]); Hu et al. (ref. [35]); Dehydrated oceanic crust from Huang et al. (ref. [36]).

References

1. Tomascak, P. B., Langmuir, C. H., le Roux, P. J. & Shirey, S. B. Lithium isotopes in global mid-ocean ridge basalts. *Geochim. Cosmochim. Acta.* **72(6),** 1626–1637 (2008).

2. Marschall, H. R., Wanless, V. D., Shimizu, N., Pogge von Strandmann, P. A. E., Elliott, T. & Monteleone, B. D. The boron and lithium isotopic composition of mid-ocean ridge basalts and the mantle. *Geochim. Cosmochim. Acta.* **207,** 102–138 (2017).

3. Ryan, J. G. & Kyle, P. R. Lithium abundance and lithium isotope variations in mantle sources: insights from intraplate volcanic rocks from Ross Island and Marie Byrd Land (Antarctica) and other oceanic islands. *Chem. Geol.* **212,** 125–142 (2004).

4. Krienitz, M. S., Garbe-schönberg, C. D., Romer, R. L., Meixner, A., Haase, K. M. & Stroncik, N. A. Lithium isotope variations in ocean Island Basalts–implications for the development of

mantle heterogeneity. *J Petrol.* **53,** 2333–2347 (2012).

5. Tang, M., Rudnick, R. L. & Chauvel, C. Sedimentary input to the source of Lesser Antilles lavas: A Li perspective. *Geochim. Cosmochim. Acta.* **144,** 43–58 (2014).

6. Hanna, H. D., Liu, X. M., Park, Y. R., Kay, S. M. & Rudnick, R. L. Lithium isotopes may trace subducting slab signatures in Aleutian arc lavas and intrusions. *Geochim. Cosmochim. Acta.* **278,** 322–339 (2020).

7. Liu, H. Y., Xiao, Y. L., Sun, H., Tong, F. T., Heuser, A., Churikova, T. & Wörner, G. Trace elements and Li isotope compositions across the Kamchatka arc: Constraints on slab‐derived fluid sources. *J Geophys Res-sol Ea.* **125,** e2019JB019237 (2020).

8. Bouman, C., Elliott, T. & Vroon, P. Z. Lithium inputs to subduction zones. *Chem. Geol.* **212,** 59–79 (2004).

9. Brens Jr, R., Liu, X. M., Turner, S. & Rushmer, T. Lithium isotope variations in Tonga–Kermadec arc–Lau back-arc lavas and Deep Sea Drilling Project (DSDP) Site 204 sediments. *Island Arc.* **28,** e12276 (2019).

10. Lechler, M., PoggevonStrandmann, P. A. E., Jenkyns, H. C., Prosser, G. & Parente, M. Lithium-isotope evidence for enhanced silicate weathering during OAE1a (Early Aptian Selli event). *Earth Planet. Sci. Lett.* **432,** 210–222 (2015).

11. Sun, H., Xiao, X. L., Gao, Y. J., Zhang, G. J., Casey, J. F. & Shen, Y. A. Rapid enhancement of chemical weathering recorded by extremely light seawater lithium isotopes at the Permian–Triassic boundary. *PNAS.* **115,** 3782–3787 (2018).

12. Murphy, J. G., Ahm, A. C., Swart, P. K. & Higgins, J. A. Reconstructing the lithium isotopic composition (δ7Li) of seawater from shallow marine carbonate sediments. *Geochim. Cosmochim. Acta.* **337,** 140–154 (2022).

13. Wei, G. Y. et al. A 13 million-year record of Li isotope compositions in island carbonates: Constraints on bulk inorganic carbonate as a global seawater Li isotope archive. *Geochim. Cosmochim. Acta.* **344,** 59–72 (2023).

14. Marschall, H. R., Pogge von Strandmann, P. A. E., Seitz, H., Elliott, T. & Niu, Y. L. The lithium isotopic composition of orogenic eclogites and deep subducted slabs. *Earth Planet. Sci. Lett.*

262, 563–580 (2007).

15. Wiechert, U. & Halliday, A. N. Non-chondritic magnesium and the origins of the inner terrestrial planets. *Earth Planet. Sci. Lett.* **256,** 360–371 (2007).

16. Bourdon, B., Tipper, E. T., Fitoussi, C. & Stracke, A. Chondritic Mg isotope composition of the Earth. *Geochim. Cosmochim. Acta.* **74,** 5069–5083 (2010).

17. Teng, F. Z., Li, W. Y., Ke, S., Marty, B., Dauphas, N., Huang, S. C., Wu, F. Y. & Pourmand, A. Magnesium isotopic composition of the Earth and chondrites. *Geochim. Cosmochim. Acta.* **74,** 4150–4166 (2010).

18. Hong, Y. D., Wu, T., Li, C. F., Chen, X. G., Lu, J. G., Gu, H. O. & Xu, R. Revisiting the South China Sea MORBs: Mg isotope and whole-rock geochemical constraints. *Marine Geology.* **465,** 107164 (2023).

19. Zhong, Y., Chen, L. H., Wang, X. J., Zhang, G. L., Xie, L. W. & Zeng, G. Magnesium isotopic variation of oceanic island basalts generated by partial melting and crustal recycling. *Earth Planet. Sci. Lett.* **463,** 127–135 (2017).

20. Wang, X. J. et al. Magnesium isotopic fractionation during basalt differentiation as recorded by evolved magmas. *Earth Planet. Sci. Lett.* **565,** 116954 (2021).

21. Teng, F. Z., Hu, Y. & Chauvel, C. Magnesium isotope geochemistry in arc volcanism. *PNAS.* **113,** 7082–7087 (2016).

22. Li, S. G. et al. Deep carbon cycles constrained by a large-scale mantle Mg isotope anomaly in eastern China. *Natl Sci Rev.* **4,** 111–120 (2017).

23. Brewer, A. W., Teng, F. Z. & Mullen, M. Magnesium isotopes as a tracer of crustal materials in volcanic arc magmas in the Northern Cascade Arc. *Front. Earth Sci.* **6,** 21 (2018).

24. Ding, Y. et al. Magnesium isotopic composition of back-arc basin lavas and its implication for the recycling of serpentinite-derived fluids. *Marine Geology.* **453,** 106921 (2022).

25. Yuan, S., Li, H., Arculus, R. J., He, Y. S., Ke, S. & Sun, W. D. Heavy magnesium isotopic compositions of basalts erupted during arc inception: Implications for the mantle source underlying the nascent Izu–Bonin–Mariana arc. *Geochim. Cosmochim. Acta.* **352,** 14–23 (2023).

26. Li, W. -Y., Teng, F. -Z., Ke, S., Rudnick, R. L., Gao, S., Wu, F. -Y. & Chappell, B. W.

Heterogeneous magnesium isotopic composition of the upper continental crust. *Geochim. Cosmochim. Acta.* **74,** 6867-6884 (2010).

27. Huang, K. J., Teng, F. Z., Elsenouy A., Li, W. Y. & Bao, Z. Y. Magnesium isotopic variations in loess: Origins and implications. *Earth Planet. Sci. Lett.* **374,** 60-70 (2013).

28. Qu, Y. R., Liu, S. A., Wu, H. C., Li, M. L. & Tian, H. C. Tracing carbonate dissolution in subducting sediments by zinc and magnesium isotopes. *Geochim. Cosmochim. Acta.* **319,** 56–72 (2022).

29. Geske, A., Zorlu, J., Richter, D. K., Buhl, D., Niedermayr, A. & Immenhauser, A. Impact of diagenesis and low grademetamorphosis on isotope (δ26Mg, δ13C, δ18O and 87Sr/86Sr) and elemental (Ca, Mg, Mn, Fe and Sr) signatures of Triassic sabkha dolomites. *Chem. Geol.* **332–333,** 45–64 (2012).

30. Fantle, M. S. & Higgins, J. The effects of diagenesis and dolomitization on Ca and Mg isotopes in marine platform carbonates: Implications for the geochemical cycles of Ca and Mg. *Geochim. Cosmochim. Acta.* **142,** 458–481 (2014).

31. Kasemann, S. A., PoggevonStrandmann, P. A. E., Prave, A. R., Fallick, A. E., Elliott, T. & Hoffmann, K. Continental weathering following a Cryogenian glaciation: Evidence from calcium and magnesium isotopes. *Earth Planet. Sci. Lett.* **396,** 66–77 (2014).

32. Liu, C., Wang, Z. R., Raub, T. D., Macdonald, F. A. & Evans, D. A. D. Neoproterozoic cap–dolostone deposition in stratified glacial meltwater plume. *Earth Planet. Sci. Lett.* **404,** 22–32 (2014).

33. Higgins, J. A. & Schrag, D. P. The Mg isotopic composition of Cenozoic seawater – evidence foralink between Mg-clays, seawater Mg/Ca, and climate. *Earth Planet. Sci. Lett.* **416,** 73–81 (2015).

34. Peng, Y. et al. Constraining dolomitization by Mg isotopes: A case study from partially dolomitized limestones of the middle Cambrian Xuzhuang Formation, North China. *Geochem Geophy Geosy*. **17,** 1109–1129 (2016).

35. Hu, Z. Y. et al. Mg isotope evidence for restriction events within the Paleotethys ocean around the Permian–Triassic transition. *Earth Planet. Sci. Lett.* **556,** 116704 (2021).

36. Huang, K. J., Teng, F. Z., Plank, T., Staudigel, H., Hu, Y. & Bao, Z. Y. Magnesium isotopic composition of altered oceanic crust and the global Mg cycle. *Geochim. Cosmochim. Acta.* **238,** 357–373 (2018).

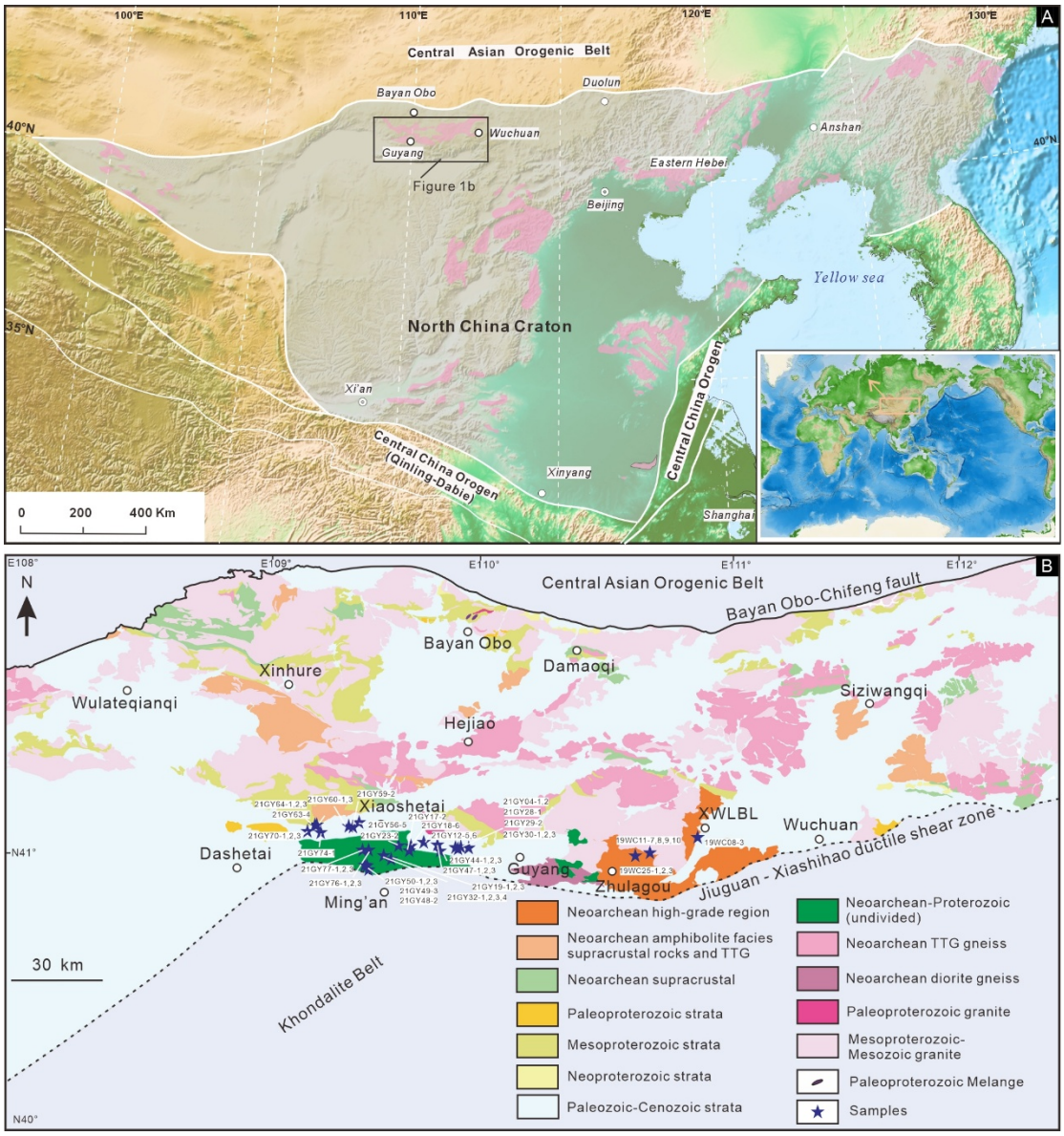

418

419 **Supplementary Text S1-Fig. 1 |** (A) Simplified sketch map showing distribution of the Archean

420 rocks in the NCC, modified from Wan et al. (ref. [42]); (B) Simplified geological map of the Yinshan

421 Block showing rock assemblages and sample locations, modified from Wang et al. (ref. [7]).

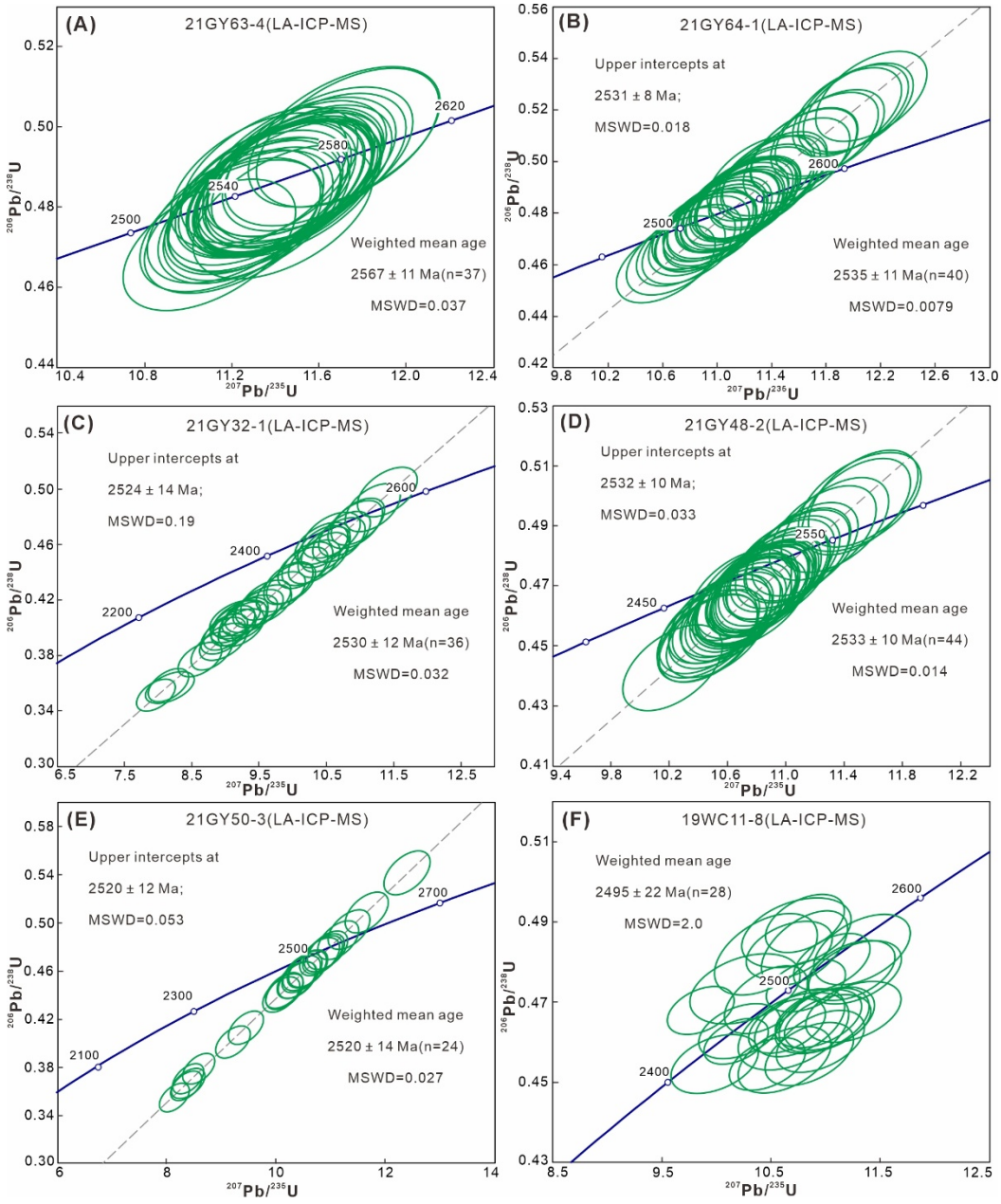

Supplementary Text S1-Fig. 2 | Zircon U-Th-Pb concordia diagrams for the Neoarchean basalts from Yinshan Block of the NCC.

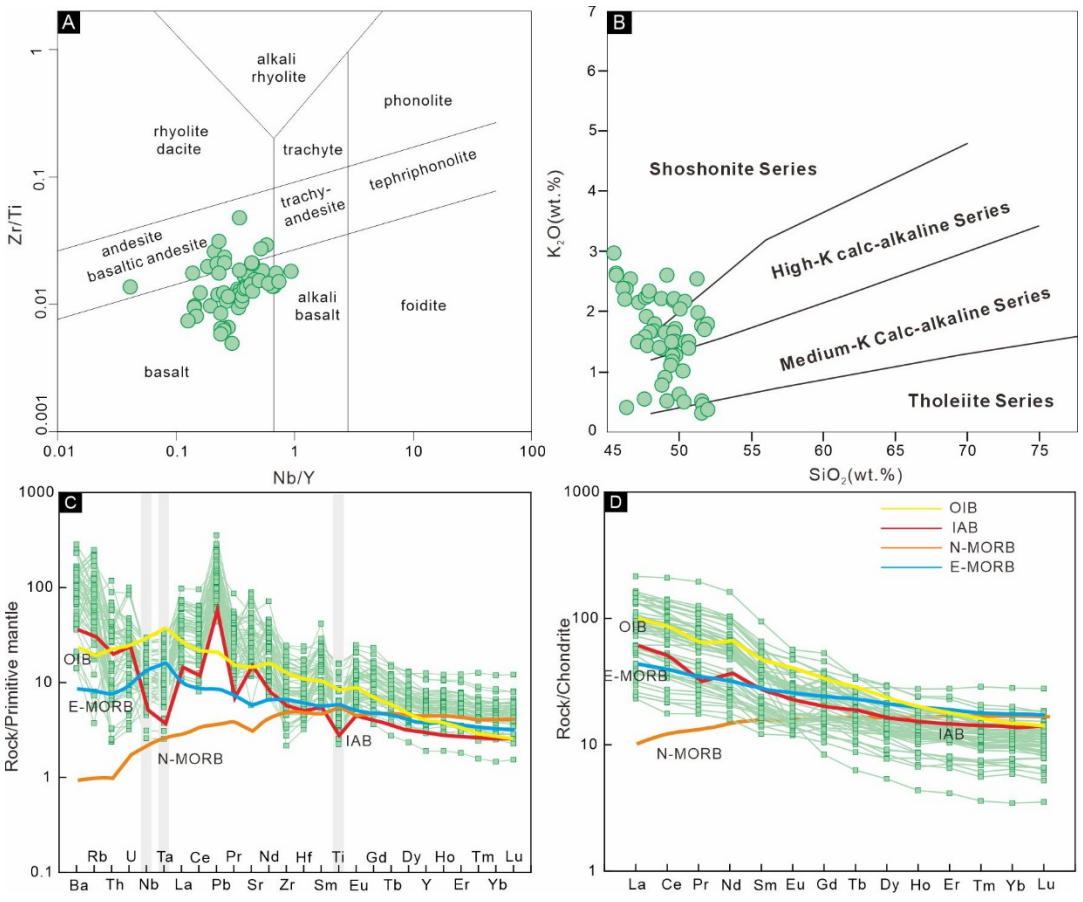

425

426 **Supplementary Text S1-Fig. 3 |** Major-trace elements composition of Neoarchean basalts from
427 Yinshan Block of the NCC. Plots of (A) Zr/Ti versus Nb/Y (modified from ref. [43]), (B) K_2O versus
428 SiO_2 (modified from ref. [44]), (C) Primitive-mantle-normalized trace element patterns and (D)
429 chondrite-normalized REE patterns. Normalized primitive mantle and chondrite values are from ref.
430 [8, 45].

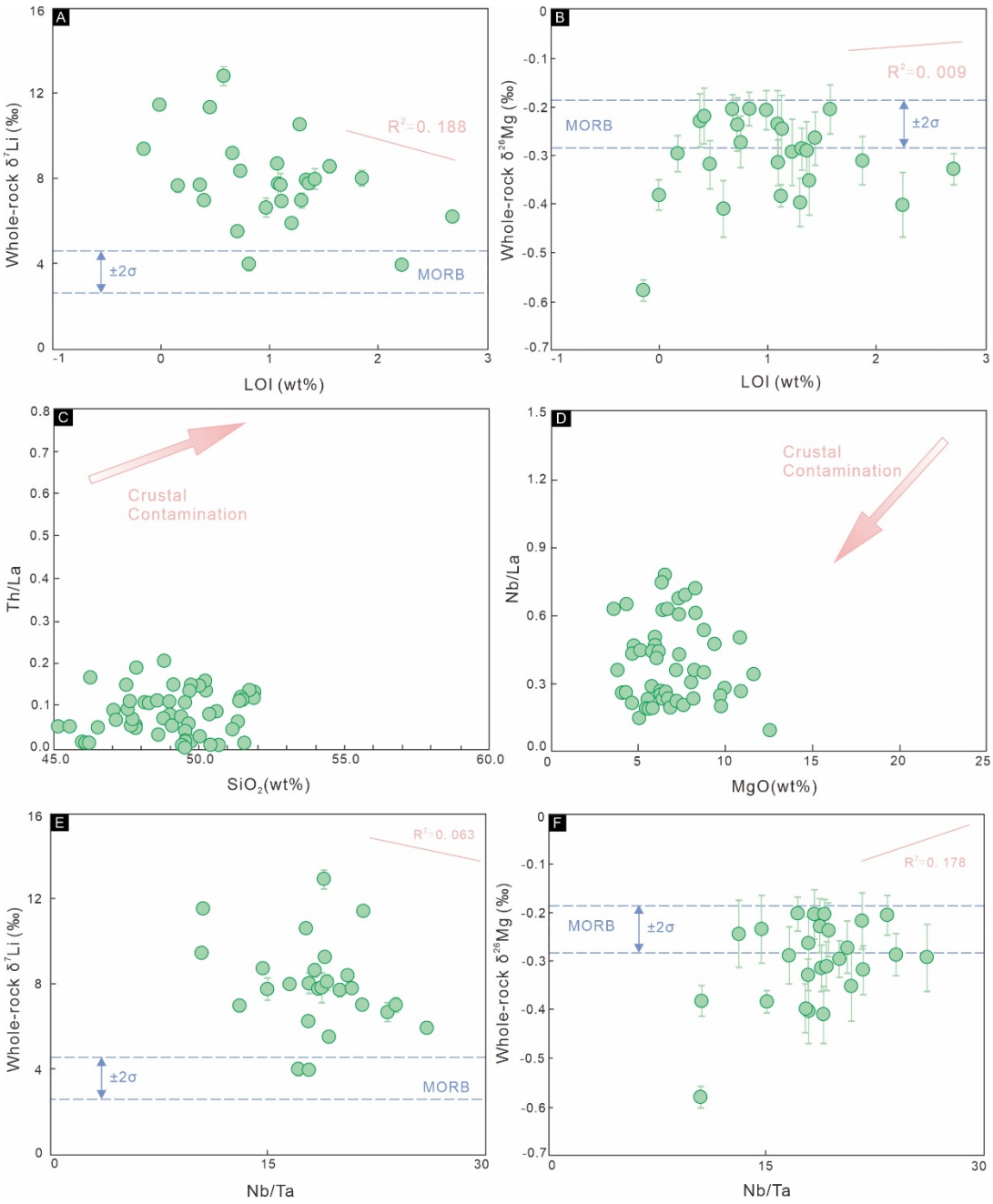

431

432 **Supplementary Text S1-Fig. 4 |** Evaluation of alteration and crustal contamination effects for the

433 Neoarchean basalts. Plots of (A) $\delta^{7}Li$ versus LOI, (B) $\delta^{26}Mg$ versus LOI, (C) Th/La versus SiO_2,

434 (D) Nb/La versus MgO, (E) $\delta^{7}Li$ versus Nb/Ta and (F) $\delta^{26}Mg$ versus Nb/Ta.

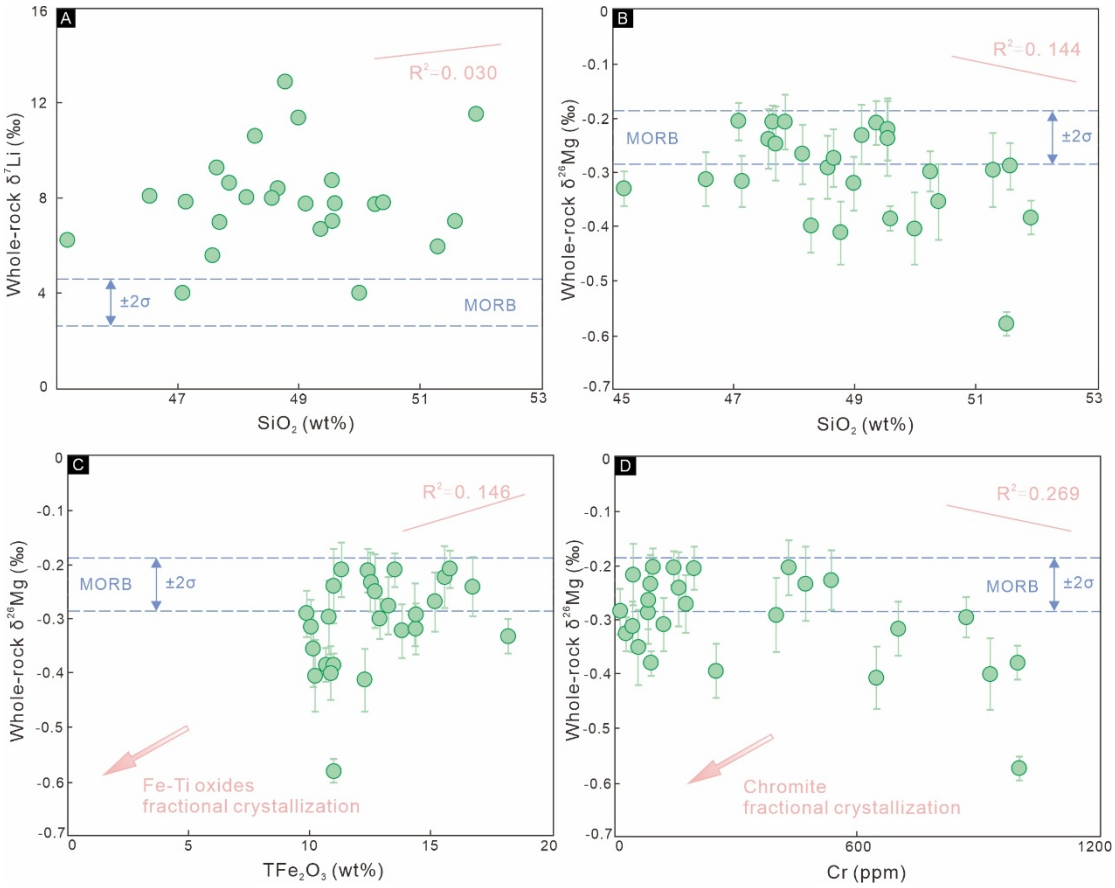

435

436 **Supplementary Text S1-Fig. 5 |** Li-Mg isotope versus fractional crystallization proxies for the

437 Neoarchean basalts. Plots of (A) $\delta^{7}Li$ versus SiO_2, (B) $\delta^{26}Mg$ versus SiO_2, (C) $\delta^{26}Mg$ versus TFe_2O_3

438 and (D) $\delta^{26}Mg$ versus Cr.

439

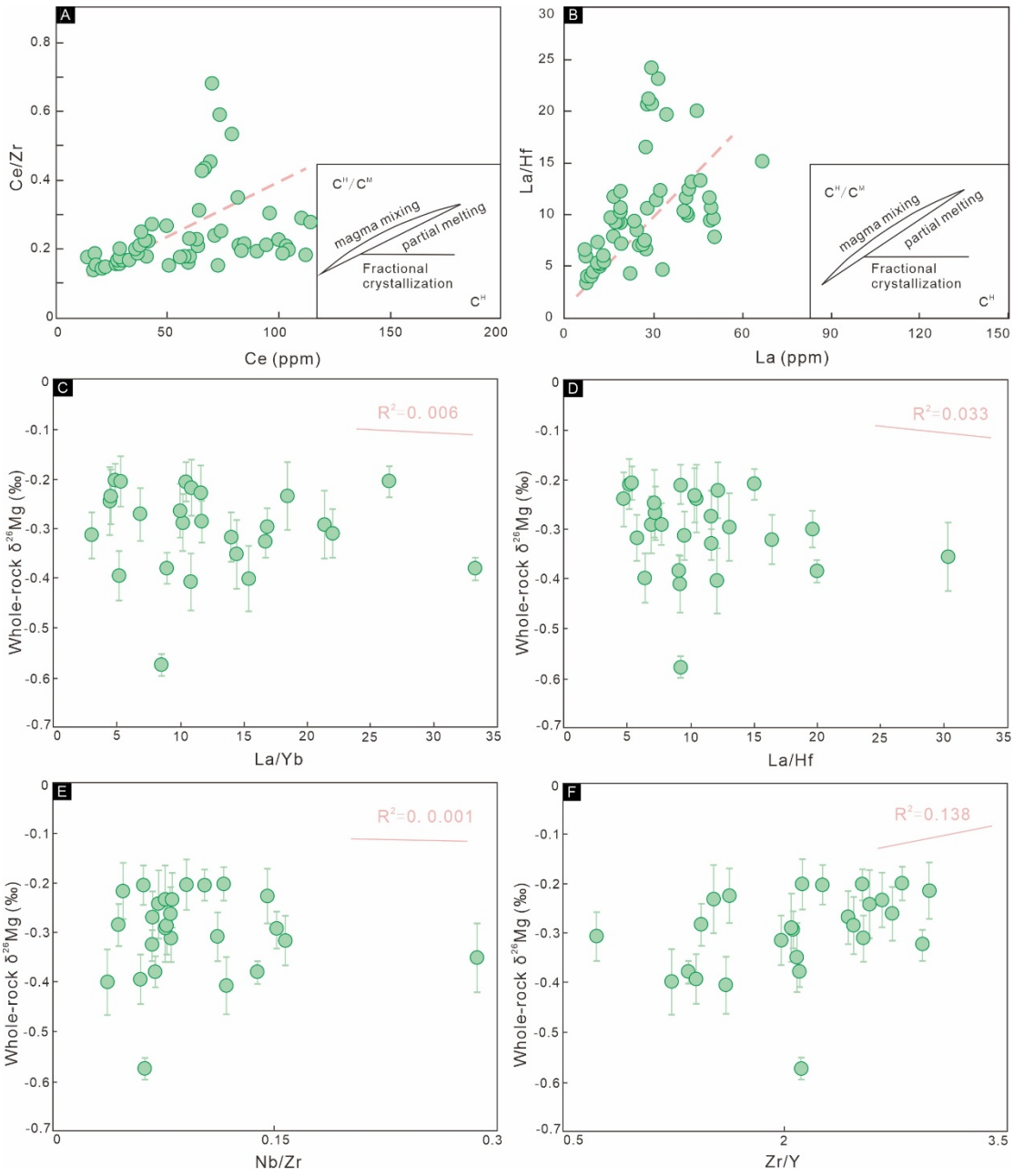

Supplementary Text S1-Fig. 6 | δ^{26}Mg versus partial melting proxies for the Neoarchean basalts. Plots of (A) Ce/Zr versus Ce (modified from ref. [19]), (B) La/Hf versus La (modified from ref. [19]), (C) δ^{26}Mg versus La/Yb, (D) δ^{26}Mg versus La/Hf, (E) δ^{26}Mg versus Nb/Zr and (F) δ^{26}Mg versus Zr/Y.

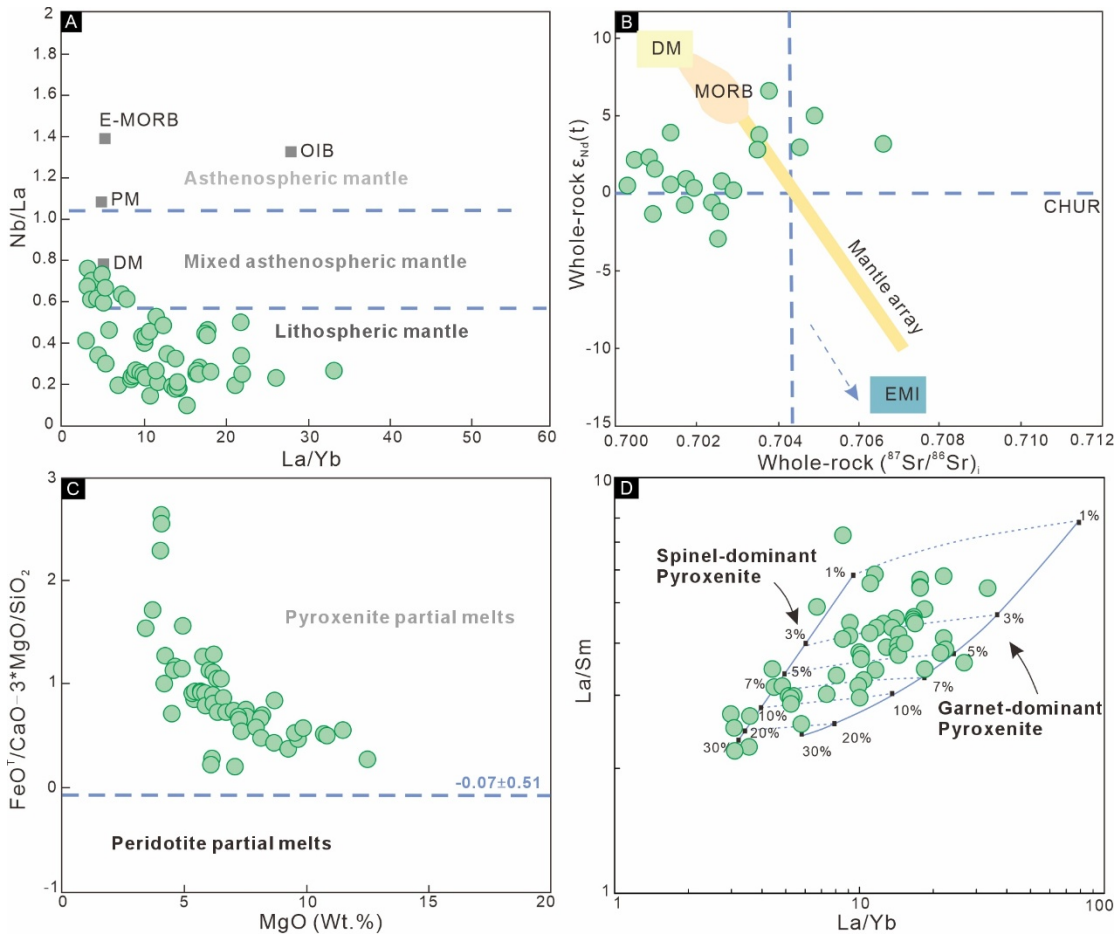

446

447 **Supplementary Text S1-Fig. 7 |** Mantle source for the studied Neoarchean basalts. Plots of (A)

448 Nb/La versus La/Yb (modified from ref. [21]); (B) whole-rock $\varepsilon_{Nd}(t)$ versus whole-rock $(^{87}Sr/^{86}Sr)_i$,

449 (C) $FeO^T/(CaO-3\times MgO/SiO_2)$ versus MgO and (D) La/Sm versus La/Yb.

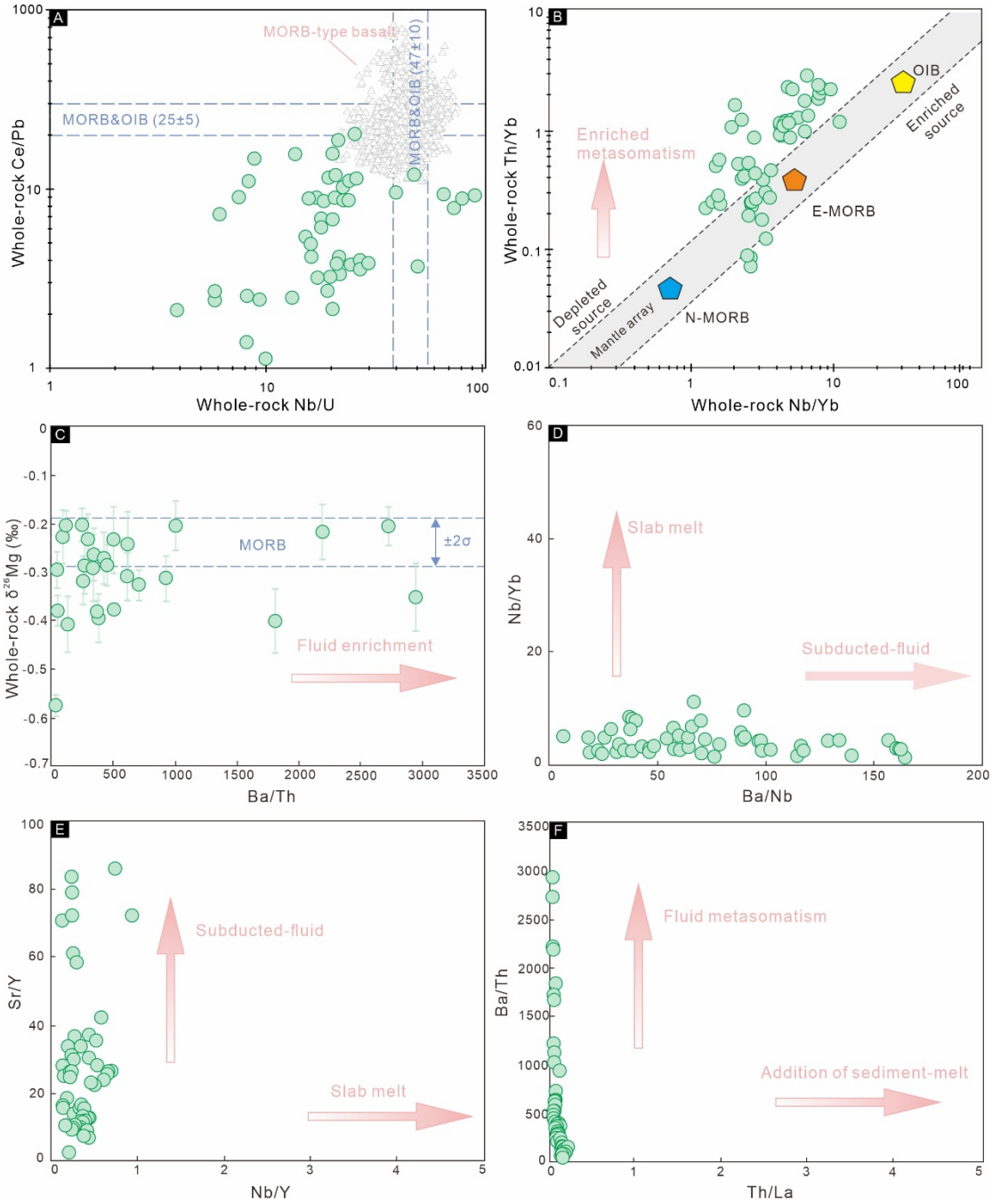

Supplementary Text S1-Fig. 8 | Discrimination diagrams for subducted fluid activity. Plots of (A) Ce/Pb versus Nb/U, (B) Th/Yb versus Nb/Yb, (C) δ^{26}Mg versus Ba/Th, (D) Nb/Yb versus Ba/Nb, (E) Sr/Y versus Nb/Y and (F) Ba/Th versus Th/La.

Table S1. Major (wt.%) and trace element (ppm) compositions of Neoarchean basalts in this study.

	21GY70-1	21GY63-4	21GY64-1	21GY74-1	21GY70-2	21GY70-3	21GY64-2	21GY64-3	21GY56-5	21GY59-2	21GY60-1
SiO_2	49.35	47.64	49.58	49.98	50.62	49.67	50.32	48.73	47.69	49.53	51.27
TiO_2	0.881	1.287	1.037	0.484	0.92	0.70	0.95	1.00	0.766	0.785	1.030
Al_2O_3	15.53	14.73	16.34	10.66	16.36	16.02	15.27	14.50	15.15	12.47	11.40
TFe_2O_3	12.39	13.48	10.98	10.20	11.23	11.11	10.28	11.22	12.68	10.97	10.78
MnO	0.160	0.139	0.123	0.150	0.14	0.14	0.15	0.16	0.168	0.156	0.145
MgO	6.62	6.26	5.68	12.49	6.18	6.74	7.00	8.16	8.68	10.81	9.64
CaO	8.78	7.97	7.75	9.01	8.05	8.97	7.98	8.75	8.23	8.55	9.45
Na_2O	3.301	3.866	4.105	1.685	3.70	3.46	3.86	3.35	3.247	2.749	2.935
K_2O	1.122	2.234	2.193	2.047	1.41	1.27	2.18	2.23	1.927	2.204	1.999
P_2O_5	0.367	0.992	0.715	0.355	0.39	0.44	0.55	0.54	0.076	0.348	0.514
LOI	0.97	0.66	1.10	2.22	0.97	0.95	0.91	1.02	1.11	1.07	1.21
Li	13.4	19.2	24.7	20.4	15.84	13.93	27.78	26.50	23.4	17.1	27.2
Ba	549	939	1164	1135	747.92	631.98	1016.21	970.22	457	679	845
Rb	22.5	116	146	61.7	30.82	27.59	137.99	135.11	44.0	85.0	121
Sr	602	1113	1501	937	667.71	716.21	1046.62	990.94	253	624	834
Zr	91.5	160	93.6	50.4	115.62	97.01	163.69	160.50	55.8	98.9	114
Nb	5.59	16.4	12.9	1.85	6.38	6.18	14.53	14.73	3.99	7.49	8.64
Ni	44.7	56.8	43.4	204	39.65	77.03	81.42	120.81	219	240	103
Co	35.2	36.3	28.7	51.1	33.59	37.92	32.21	37.33	55.0	49.9	43.7
Zn	85.4	120	104	78.9	81.82	81.31	103.87	105.50	133	88.2	84.0
Cr	198	149	92.9	930	120.75	260.76	215.69	302.82	161	474	402
La	23.5	66.7	44.7	18.9	24.43	31.47	40.96	40.46	11.4	27.9	43.5
Ce	59.9	169	96.0	42.8	63.84	74.36	94.41	100.17	28.5	63.3	111

Pr	8.25	23.8	11.7	5.60	9.02	9.30	12.49	13.55	3.76	7.73	14.7
Nd	34.1	96.9	45.0	23.2	37.80	36.67	51.10	55.87	14.8	30.7	58.9
Sm	7.13	18.4	8.12	4.69	8.02	7.13	9.82	11.49	3.24	5.69	11.3
Eu	1.68	4.16	2.64	1.45	1.89	1.88	2.64	2.85	1.03	1.57	2.02
Gd	5.87	13.7	6.40	4.02	6.79	5.87	8.03	9.11	3.77	4.81	8.34
Tb	0.82	1.63	0.76	0.52	0.89	0.79	1.00	1.14	0.66	0.60	1.04
Dy	4.32	7.96	3.72	2.71	5.10	4.39	5.16	5.85	4.20	3.39	5.04
Ho	0.88	1.29	0.62	0.50	0.95	0.83	0.87	1.02	0.88	0.62	0.90
Er	2.24	3.39	1.49	1.37	2.54	2.25	2.19	2.63	2.68	1.69	2.43
Tm	0.33	0.40	0.20	0.18	0.36	0.33	0.29	0.33	0.40	0.23	0.31
Yb	2.25	2.52	1.34	1.23	2.43	2.32	1.86	2.19	2.57	1.51	2.04
Lu	0.32	0.35	0.19	0.17	0.33	0.33	0.27	0.31	0.38	0.20	0.29
Y	24.1	37.0	17.4	13.2	26.02	23.94	24.91	28.11	24.7	16.9	24.8
Cs	0.19	1.90	5.64	0.90	0.22	0.23	4.51	5.13	0.95	1.64	2.30
Ta	0.24	0.86	0.87	0.10	0.23	0.36	0.92	0.87	0.31	0.51	0.33
Hf	2.54	4.42	2.24	1.56	2.93	2.76	4.04	3.94	1.58	2.65	3.32
Th	0.20	7.58	3.11	0.63	0.21	0.54	3.54	2.99	0.74	1.34	2.48
U	0.067	1.84	2.10	0.20	0.10	0.15	1.91	1.76	0.25	0.38	0.63
Ga	20.8	23.1	22.5	13.6	21.83	21.60	21.66	20.82	16.6	16.4	18.6
Pb	6.44	11.4	13.2	17.8	6.78	7.75	10.25	9.03	5.74	5.41	6.99
	21GY60-3	21GY77-1	21GY76-1	21GY76-2	21GY76-3	21GY77-2	21GY77-3	21GY48-2	21GY50-3	21GY49-3	21GY50-1
SiO_2	49.07	50.38	46.18	46.11	46.03	49.51	49.44	46.53	48.26	49.68	49.49
TiO_2	1.37	0.825	1.10	1.04	1.04	0.93	0.88	0.669	0.782	0.94	1.16
Al_2O_3	11.26	18.07	18.01	17.93	17.97	17.36	16.86	17.11	16.53	17.02	13.78
TFe_2O_3	11.32	10.14	12.39	11.84	11.83	10.78	10.80	10.04	10.85	10.71	14.00

MnO	0.15	0.129	0.14	0.14	0.14	0.14	0.14	0.130	0.170	0.18	0.22
MgO	9.53	5.41	5.67	5.45	5.33	6.20	6.39	10.74	7.94	5.85	6.47
CaO	9.29	7.78	8.49	8.26	8.53	8.28	8.68	7.55	9.08	8.34	8.75
Na_2O	2.58	4.151	3.28	3.54	3.25	3.66	3.83	2.640	3.401	3.42	3.68
K_2O	2.62	1.497	2.38	2.22	2.40	1.27	1.16	2.554	1.790	1.72	1.51
P_2O_5	0.56	0.412	0.50	0.48	0.48	0.42	0.40	0.152	0.091	0.10	0.11
LOI	2.20	1.36	1.69	2.23	2.12	0.76	0.78	1.85	1.28	2.21	0.87
Li	30.27	25.2	29.38	29.13	28.01	14.02	10.16	22.9	17.8	21.10	10.78
Ba	1041.33	804	926.25	861.86	892.96	554.12	472.63	536	310	522.99	290.38
Rb	157.50	40.1	54.79	52.92	58.39	24.66	20.13	136	107	66.56	75.85
Sr	573.01	1343	1692.77	1865.91	1781.42	1134.02	994.09	620	367	464.94	245.25
Zr	127.93	24.1	39.25	39.81	39.70	36.43	30.62	72.3	37.5	59.30	82.79
Nb	11.78	6.91	5.78	5.34	5.51	8.62	7.84	8.04	2.22	9.07	6.30
Ni	121.42	33.9	32.54	31.20	31.01	49.90	51.03	257	154	95.67	50.45
Co	44.13	31.3	36.57	33.64	34.87	34.88	36.91	59.1	51.0	45.97	50.70
Zn	128.07	90.6	102.33	94.06	93.96	99.26	96.32	92.9	74.0	80.79	106.54
Cr	452.98	60.7	47.69	42.21	41.11	126.30	143.71	123	253	26.64	58.87
La	46.08	30.0	29.27	28.16	28.78	31.78	29.46	15.9	7.18	19.01	9.91
Ce	114.45	70.2	69.42	65.18	66.12	78.99	74.51	28.7	14.2	49.71	22.07
Pr	15.33	9.23	9.19	8.43	8.56	10.93	10.27	3.53	2.14	7.48	3.19
Nd	61.87	35.8	37.52	34.58	35.75	44.76	42.28	13.7	9.51	32.66	13.76
Sm	11.77	7.02	7.64	7.19	7.16	9.10	9.28	2.70	2.37	7.35	3.66
Eu	2.00	1.83	2.05	1.94	1.96	1.93	1.85	1.07	0.87	1.85	1.12
Gd	8.79	5.82	6.08	5.73	5.64	7.48	7.60	2.16	2.70	6.66	4.33
Tb	1.05	0.82	0.86	0.82	0.82	1.13	1.14	0.30	0.41	0.98	0.72

Dy	5.53	4.56	4.60	4.24	4.35	5.94	6.29	1.73	2.51	6.12	4.70
Ho	0.95	0.89	0.91	0.80	0.86	1.15	1.20	0.31	0.56	1.22	1.02
Er	2.53	2.34	2.35	2.35	2.27	3.05	3.26	0.87	1.60	3.45	2.89
Tm	0.33	0.32	0.31	0.30	0.31	0.42	0.43	0.12	0.24	0.52	0.43
Yb	2.06	2.08	2.04	1.97	2.00	2.74	2.97	0.72	1.40	3.27	2.77
Lu	0.29	0.28	0.28	0.26	0.28	0.37	0.38	0.11	0.21	0.49	0.43
Y	25.47	23.0	23.45	22.24	22.53	31.13	32.32	8.59	14.8	34.05	27.48
Cs	3.10	1.05	2.26	2.25	2.35	0.40	0.42	6.84	1.34	0.46	0.42
Ta	0.39	0.33	0.27	0.26	0.30	0.42	0.41	0.42	0.13	0.70	0.50
Hf	3.46	0.99	1.41	1.37	1.36	1.37	1.22	1.66	1.10	1.78	2.30
Th	2.70	0.27	0.55	0.50	0.52	0.50	0.22	0.87	0.81	2.91	1.12
U	0.54	0.093	0.21	0.19	0.18	0.18	0.08	0.61	0.58	0.37	0.76
Ga	19.90	23.7	25.40	24.29	24.38	23.56	23.43	15.8	16.2	20.54	18.26
Pb	9.31	8.89	17.40	17.53	17.73	6.39	8.01	11.7	6.82	4.44	8.73
	21GY50-2	21GY19-1	21GY32-1	21GY32-2	21GY19-2	21GY19-3	21GY32-3	21GY32-4	21GY23-2	21GY17-2	21GY44-3
SiO_2	49.62	47.84	48.55	48.13	47.73	47.83	48.97	50.58	51.55	47.80	45.18
TiO_2	1.17	1.194	1.798	1.890	1.22	1.22	1.81	2.73	0.660	1.24	3.408
Al_2O_3	13.74	16.17	14.25	13.99	15.55	14.58	14.23	13.18	18.47	16.77	13.06
TFe_2O_3	13.79	11.28	14.31	15.12	11.56	13.02	14.42	15.90	9.87	14.50	18.15
MnO	0.23	0.176	0.204	0.190	0.18	0.19	0.19	0.20	0.178	0.21	0.203
MgO	6.37	7.23	6.14	5.77	7.32	8.19	6.01	3.70	4.45	8.07	4.08
CaO	8.67	9.28	8.61	8.39	10.47	9.83	8.63	7.41	9.22	2.32	5.79
Na_2O	3.71	2.230	3.000	2.561	2.22	1.99	2.76	2.45	4.043	2.95	2.283
K_2O	1.52	2.345	1.425	1.688	1.44	1.66	1.67	1.53	0.459	2.28	2.993
P_2O_5	0.11	0.225	0.463	0.500	0.22	0.23	0.47	1.00	0.264	0.07	1.377

LOI	0.93	1.56	1.34	1.42	1.58	1.53	1.33	0.86	1.29	3.13	2.69
Li	11.22	11.0	9.41	10.3	12.08	14.42	9.25	7.80	5.66	26.90	11.7
Ba	272.21	597	794	1081	312.82	387.49	1066.90	997.93	127	842.68	1983
Rb	77.77	39.0	27.1	37.5	18.41	19.55	34.39	35.00	5.05	49.05	89.2
Sr	256.13	334	440	353	341.12	261.80	384.97	357.00	867	121.18	329
Zr	85.41	84.1	144	153	95.07	92.12	145.63	268.71	82.9	192.23	189
Nb	7.15	7.60	11.0	12.1	7.32	8.02	11.04	18.40	3.67	12.00	12.7
Ni	52.65	81.8	82.9	78.4	78.28	83.87	81.91	30.02	20.9	113.74	37.5
Co	50.53	40.2	45.1	43.8	39.40	43.38	46.43	37.54	26.1	48.45	52.0
Zn	105.24	104	134	149	105.54	123.21	144.79	139.99	72.9	85.76	192
Cr	57.08	432	85.5	84.4	395.08	488.10	81.79	11.64	16.3	212.67	30.4
La	9.14	11.2	25.0	27.2	11.93	13.08	26.46	50.77	16.7	50.50	48.9
Ce	20.69	27.7	55.7	60.1	28.58	33.03	57.68	112.22	36.8	90.30	103
Pr	3.01	3.84	6.94	7.48	4.02	4.40	7.45	14.30	4.78	9.69	13.2
Nd	13.33	17.0	31.4	33.6	17.85	19.46	32.25	62.00	20.2	36.74	57.4
Sm	3.61	3.86	6.72	7.05	3.98	4.27	6.95	12.79	3.80	6.84	10.7
Eu	1.13	1.23	2.14	2.26	1.27	1.29	2.23	3.75	1.18	1.94	3.46
Gd	4.43	3.87	6.10	6.59	4.23	4.31	6.42	11.78	3.20	7.38	9.42
Tb	0.75	0.61	0.94	0.99	0.67	0.72	0.94	1.64	0.48	1.32	1.18
Dy	5.05	3.84	5.23	5.69	4.14	4.16	5.41	9.52	2.49	9.17	6.82
Ho	1.06	0.72	1.03	1.09	0.78	0.80	1.04	1.71	0.48	1.98	1.34
Er	3.02	2.25	2.91	3.15	2.41	2.44	3.04	4.82	1.48	5.82	3.60
Tm	0.44	0.32	0.40	0.41	0.35	0.36	0.40	0.62	0.22	0.93	0.46
Yb	2.95	2.11	2.46	2.72	2.28	2.42	2.62	3.95	1.43	5.87	2.92
Lu	0.47	0.31	0.38	0.41	0.34	0.35	0.40	0.60	0.21	0.90	0.44

Y	28.27	20.8	28.7	30.7	21.99	23.15	29.91	48.71	14.2	56.77	36.8
Cs	0.51	0.12	0.18	0.37	0.12	0.12	0.29	0.30	0.074	0.35	0.48
Ta	0.58	0.42	0.67	0.68	0.39	0.43	0.66	1.10	0.15	0.42	0.71
Hf	2.37	2.14	3.59	3.73	2.32	2.18	3.74	6.61	2.15	5.32	4.19
Th	1.25	0.59	2.92	3.11	0.89	0.75	3.01	4.86	0.28	9.98	2.78
U	0.87	0.32	0.61	0.59	0.38	0.38	0.61	0.99	0.073	0.53	0.80
Ga	18.17	17.4	18.9	19.9	18.32	17.71	18.86	24.25	19.8	22.83	23.2
Pb	14.86	6.95	8.08	8.87	10.51	8.59	9.43	13.09	9.99	8.82	19.9
	21GY12-5	21GY12-6	21GY44-1	21GY44-2	21GY47-1	21GY47-2	21GY47-3	21GY28-1	21GY30-1	21GY30-2	21GY30-3
SiO_2	49.94	50.21	45.59	45.58	51.72	51.50	51.87	47.13	47.57	48.64	47.08
TiO_2	2.79	2.35	3.45	3.36	1.76	1.80	1.76	0.91	1.38	0.89	1.38
Al_2O_3	14.42	15.37	13.19	13.04	15.97	16.18	16.14	13.70	13.41	13.93	14.35
TFe_2O_3	16.93	14.75	18.05	17.69	10.86	11.34	10.85	14.34	16.70	13.22	15.75
MnO	0.21	0.20	0.18	0.17	0.15	0.15	0.14	0.23	0.29	0.26	0.29
MgO	3.48	4.21	4.10	4.02	4.62	4.93	4.62	7.18	6.25	7.51	6.24
CaO	8.64	8.74	5.62	6.24	7.01	7.11	6.83	11.32	8.92	9.77	9.35
Na_2O	2.12	2.43	2.24	2.36	3.82	3.83	3.88	1.68	3.00	3.16	3.06
K_2O	0.64	1.03	2.65	2.62	1.71	1.78	1.80	2.17	1.59	1.42	1.50
P_2O_5	0.36	0.26	1.39	1.37	0.67	0.69	0.67	0.08	0.12	0.09	0.13
LOI	0.81	0.89	3.00	3.35	0.97	0.98	0.98	1.08	0.70	0.73	0.81
Li	5.79	6.00	10.58	10.29	10.95	11.22	11.03	4.69	9.27	10.11	11.55
Ba	134.06	263.19	1724.04	1625.01	738.59	721.36	719.51	526.46	348.72	262.06	327.84
Rb	15.69	37.94	63.46	60.03	36.87	38.54	39.93	28.50	22.28	18.34	20.99
Sr	309.83	299.37	357.64	327.36	731.40	727.50	730.87	706.36	284.93	384.28	311.13
Zr	272.10	194.10	212.35	232.90	144.59	147.01	182.71	40.17	93.67	51.01	88.50

Nb	21.07	14.64	12.87	12.62	18.51	18.82	19.59	3.20	7.55	3.44	10.20
Ni	36.48	48.14	35.73	35.84	31.85	35.55	32.05	56.18	72.89	76.32	72.92
Co	43.80	42.41	48.31	45.54	29.87	32.13	30.40	56.66	58.43	48.75	50.79
Zn	153.25	127.27	198.52	191.82	101.86	101.52	100.50	109.38	133.59	127.75	131.86
Cr	24.10	56.73	28.79	28.63	56.26	61.70	57.22	46.90	90.25	178.44	96.74
La	33.37	22.43	49.22	49.17	42.08	41.27	41.72	7.56	11.93	16.56	13.54
Ce	72.81	50.89	104.57	101.77	84.55	82.29	83.35	17.56	27.07	38.43	29.89
Pr	9.36	6.52	13.43	13.24	10.24	10.20	10.16	2.30	3.33	4.23	3.64
Nd	40.47	28.46	58.58	57.25	39.93	39.01	39.11	10.66	14.33	15.21	15.75
Sm	9.88	7.39	10.70	10.47	7.55	7.43	7.25	2.76	3.76	3.28	4.24
Eu	2.74	2.08	3.48	3.47	2.19	2.22	2.15	0.89	1.14	1.10	1.31
Gd	9.92	6.91	9.57	9.45	6.57	6.56	6.48	3.54	4.27	3.43	4.51
Tb	1.58	1.13	1.30	1.25	0.92	0.94	0.91	0.62	0.69	0.58	0.76
Dy	9.39	6.76	6.88	6.86	5.47	5.30	5.15	4.04	4.56	3.98	4.85
Ho	1.74	1.27	1.37	1.34	1.08	1.02	1.00	0.84	0.96	0.79	0.99
Er	5.06	3.78	3.74	3.68	2.91	2.77	2.77	2.59	2.73	2.46	2.86
Tm	0.67	0.48	0.49	0.47	0.41	0.39	0.39	0.39	0.40	0.37	0.41
Yb	4.18	3.06	2.98	2.97	2.37	2.34	2.34	2.53	2.65	2.42	2.79
Lu	0.58	0.43	0.46	0.46	0.36	0.36	0.35	0.37	0.39	0.37	0.41
Y	48.52	34.93	37.04	36.85	28.67	27.95	27.85	25.18	27.13	24.20	27.76
Cs	0.12	0.10	0.22	0.21	0.61	0.72	0.75	0.14	0.04	0.05	0.04
Ta	1.35	0.96	0.69	0.67	1.15	1.13	1.19	0.17	0.39	0.17	0.60
Hf	7.40	5.37	4.62	5.25	3.39	3.59	4.23	1.29	2.48	1.42	2.48
Th	5.26	3.67	2.77	2.79	5.91	4.98	5.43	0.57	1.16	0.61	1.30
U	0.93	0.63	0.79	0.78	0.89	0.78	0.85	0.32	0.39	0.15	0.46

Ga	27.28	24.55	23.93	22.89	20.42	20.68	20.70	16.74	20.21	17.03	21.57
Pb	17.38	12.34	25.09	20.35	9.36	9.49	9.57	16.13	8.37	9.24	8.91
	21GY04-1	21GY04-2	21GY29-2	19WC08-3	19WC11-7	19WC11-8	19WC11-9	19WC11-10	19WC25-1	19WC25-2	
SiO_2	46.29	47.52	49.40	49.54	50.24	48.98	48.76	49.10	51.90	51.50	
TiO_2	1.41	1.36	1.74	1.75	0.76	0.80	0.77	0.80	0.56	0.55	
Al_2O_3	15.67	13.16	16.93	13.80	12.87	11.58	12.68	13.52	11.12	9.83	
TFe_2O_3	14.09	13.75	10.79	15.53	12.88	13.79	12.25	12.49	10.65	10.98	
MnO	0.19	0.18	0.15	0.19	0.19	0.21	0.20	0.20	0.72	0.69	
MgO	7.53	8.16	5.84	4.95	9.87	11.52	9.27	8.68	6.17	7.09	
CaO	10.61	12.57	7.73	7.52	10.06	9.87	11.83	11.67	15.92	16.24	
Na_2O	2.98	1.98	3.69	2.95	2.29	1.67	2.01	2.24	2.36	2.30	
K_2O	0.42	0.55	1.51	1.65	0.51	0.92	0.80	0.52	0.39	0.33	
P_2O_5	0.12	0.11	0.57	0.89	0.31	0.34	0.35	0.38	0.26	0.28	
LOI	0.51	0.71	1.58	0.40	0.16	0.45	0.58	0.36	-0.02	-0.16	
Li	7.66	10.45	48.01	12.59	7.60	7.54	7.15	7.12	14.16	20.33	
Ba	98.17	131.16	519.16	1595.92	250.89	609.64	493.19	288.81	147.36	98.44	
Rb	4.61	11.10	51.17	27.27	7.67	53.57	31.60	12.01	3.63	2.37	
Sr	891.92	621.30	727.22	519.52	282.01	262.22	360.68	389.60	547.58	394.02	
Zr	80.85	68.60	190.70	101.43	65.19	60.51	70.38	70.08	68.54	65.21	
Nb	5.28	5.84	13.89	4.81	9.85	9.51	8.24	10.15	4.75	4.06	
Ni	93.01	95.91	60.23	48.47	126.48	175.91	169.07	177.39	283.29	275.74	
Co	46.47	36.04	34.24	50.43	50.93	60.69	52.08	54.97	47.08	51.10	
Zn	72.47	75.25	87.17	110.62	92.31	96.30	77.04	78.95	249.15	692.30	
Cr	168.54	210.43	93.91	47.93	871.39	703.12	649.41	537.90	997.63	1002.57	
La	7.59	8.11	27.60	32.32	34.56	27.56	17.27	18.77	18.74	17.87	

Ce	17.43	18.52	59.54	71.42	81.71	64.44	35.64	38.04	41.53	40.50
Pr	2.54	2.71	7.28	9.39	10.06	7.96	3.92	4.16	5.20	5.16
Nd	12.10	12.49	30.26	40.29	39.94	31.61	15.40	15.66	20.51	20.90
Sm	3.40	3.51	6.11	7.53	7.61	5.93	3.05	3.16	4.44	4.30
Eu	1.06	1.11	2.00	2.60	1.03	0.96	1.00	1.03	1.24	1.04
Gd	4.02	4.17	5.57	6.72	5.74	4.99	3.05	2.99	3.96	4.18
Tb	0.76	0.75	0.78	1.03	0.81	0.74	0.50	0.50	0.69	0.67
Dy	4.11	4.45	4.63	5.74	4.32	3.89	2.91	2.96	3.88	3.89
Ho	0.91	0.90	0.85	1.17	0.84	0.81	0.62	0.62	0.76	0.79
Er	2.56	2.43	2.55	3.28	2.37	2.19	1.65	1.69	2.29	2.29
Tm	0.37	0.35	0.35	0.48	0.32	0.31	0.24	0.24	0.30	0.31
Yb	2.44	2.32	2.21	2.97	2.05	1.97	1.60	1.62	2.09	2.10
Lu	0.36	0.33	0.34	0.45	0.31	0.29	0.25	0.25	0.32	0.32
Y	26.63	24.36	25.98	33.50	23.03	21.21	16.36	16.63	21.13	21.69
Cs	0.07	0.46	1.52	0.37	0.11	1.40	1.23	0.40	0.11	0.06
Ta	0.36	0.39	0.81	0.22	0.49	0.44	0.44	0.55	0.45	0.39
Hf	2.36	2.08	4.24	2.65	1.76	1.67	1.87	1.81	2.05	1.92
Th	1.31	1.25	2.24	0.73	4.93	2.35	3.66	2.95	2.63	2.29
U	0.26	0.33	0.53	0.24	0.45	0.37	0.52	0.59	0.79	0.69
Ga	21.57	17.73	18.97	20.90	16.14	14.65	14.14	14.95	13.84	13.81
Pb	8.13	5.79	5.16	4.18	4.34	3.09	4.01	4.21	15.49	16.94

Table S2. Sr–Nd isotopes of Neoarchean basalts in this study.

Sample No.	$^{87}Rb/^{86}Sr$	$^{87}Sr/^{86}Sr$	2σ	$(^{87}Sr/^{86}Sr)i$	$^{147}Sm/^{144}Nd$	$^{143}Nd/^{144}Nd$	2σ	εNd(0)	εNd(t)
21GY70-1	0.1079	0.706885	0.000009	0.702908	0.1266	0.51148	0.00001	-22.63	0.38
21GY63-4	0.3017	0.712445	0.000008	0.701321	0.1149	0.51130	0.00001	-26.06	0.78
21GY64-1	0.2810	0.712069	0.000007	0.701707	0.1093	0.51123	0.00000	-27.50	1.18
21GY56-5	0.5025	0.713223	0.000007	0.694695	0.1323	0.51179	0.00001	-16.62	4.52
21GY59-2	0.3930	0.713829	0.000008	0.699338	0.1122	0.51132	0.00000	-25.65	2.08
21GY60-1	0.4184	0.717982	0.000008	0.702556	0.1157	0.51133	0.00000	-25.55	1.02
21GY77-1	0.0861	0.704107	0.000010	0.700933	0.1187	0.51127	0.00001	-26.69	-1.10
21GY48-2	0.6313	0.723647	0.000008	0.700367	0.1192	0.51146	0.00001	-23.04	2.40
21GY50-3	0.8400	0.734308	0.000006	0.703335	0.1510	0.51202	0.00001	-12.06	2.96
21GY19-1	0.3364	0.710164	0.000008	0.697759	0.1372	0.51184	0.00001	-15.61	3.95
21GY32-1	0.1776	0.713120	0.000011	0.706571	0.1295	0.51168	0.00001	-18.69	3.37
21GY32-2	0.3062	0.712616	0.000007	0.701327	0.1270	0.51168	0.00001	-18.79	4.10
21GY23-2	0.0168	0.704416	0.000005	0.703796	0.1139	0.51159	0.00001	-20.37	6.84
21GY44-3	0.7829	0.725780	0.000008	0.696911	0.1130	0.51141	0.00000	-23.92	3.55
21GY28-1	0.1164	0.709180	0.000007	0.704887	0.1565	0.51223	0.00001	-8.04	5.17
21GY30-1	0.2257	0.711842	0.000008	0.703520	0.1587	0.51220	0.00001	-8.60	3.89
21GY30-2	0.1377	0.709611	0.000006	0.704532	0.1306	0.51169	0.00001	-18.51	3.18
21GY30-3	0.1947	0.711750	0.000010	0.704569	0.1628	0.51213	0.00001	-9.89	1.24
19WC08-3	0.1515	0.706330	0.000007	0.700745	0.1131	0.51138	0.00001	-24.48	2.95
19WC11-7	0.5896	0.721402	0.000010	0.699660	0.1136	0.51130	0.00001	-26.16	1.11
19WC11-8	0.2529	0.710117	0.000007	0.700793	0.1197	0.51146	0.00001	-23.06	2.23
19WC11-9	0.0890	0.705178	0.000008	0.701898	0.1222	0.51143	0.00001	-23.54	0.91
19WC11-10	0.0785	0.704564	0.000006	0.701669	0.1153	0.51126	0.00001	-26.82	-0.11

19WC25-1	0.0191	0.703248	0.000010	0.702543	0.1310	0.51141	0.00001	-23.95	-2.41
19WC25-2	0.0173	0.703034	0.000008	0.702395	0.1245	0.51142	0.00000	-23.72	-0.04

Table S3. Li-Mg concentrations and isotope compositions of Neoarchean basalts in this study.

Sample	Li (ppm)	δ^{7}Li (‰)	2SD	MgO (wt. %)	δ^{26}Mg (‰)	2SD
21GY70-1	13.37	6.69	0.44	6.62	-0.207	0.040
21GY63-4	19.23	9.28	0.10	6.26	-0.206	0.031
21GY64-1	24.68	7.78	0.51	5.68	-0.383	0.022
21GY74-1	20.38	3.97	0.02	12.49	-0.402	0.066
21GY56-5	23.44	6.98	0.27	8.68	-0.245	0.068
21GY59-2	17.12	8.76	0.15	10.81	-0.236	0.069
21GY60-1	27.16	5.96	0.13	9.64	-0.293	0.069
21GY77-1	25.24	7.82	0.13	5.41	-0.353	0.070
21GY48-2	22.89	8.09	0.35	10.74	-0.311	0.049
21GY50-3	17.81	10.63	0.14	7.94	-0.397	0.050
21GY19-1	11.00	8.64	0.31	7.23	-0.206	0.051
21GY32-1	9.41	7.98	0.22	6.14	-0.289	0.058
21GY32-2	10.27	8.04	0.48	5.77	-0.265	0.055
21GY23-2	5.66	7.03	0.35	4.45	-0.287	0.043
21GY44-3	11.71	6.25	0.00	4.08	-0.328	0.031
21GY28-1	4.69	7.84	0.69	7.18	-0.315	0.047
21GY30-1	9.27	5.58	0.22	6.25	-0.237	0.055
21GY30-2	10.11	8.41	0.22	7.51	-0.272	0.053
21GY30-3	11.55	4.02	0.32	6.24	-0.204	0.034
19WC08-3	12.59	7.03	0.21	4.95	-0.219	0.057
19WC11-7	7.60	7.74	0.32	9.87	-0.297	0.037
19WC11-8	7.54	11.41	0.01	11.52	-0.318	0.050
19WC11-9	7.15	12.92	0.44	9.27	-0.410	0.058

19WC11-10	7.12	7.77	0.09	8.68	-0.229	0.055
19WC25-1	14.16	11.55	0.25	6.17	-0.382	0.031
19WC25-2	20.33	9.44	0.09	7.09	-0.577	0.022

Table S4. Summarized parameters for model calculations.

Endmembers	MgO (wt. %)	δ^{26}Mg (‰)	Sr (μg/g)	$^{87}Sr/^{86}Sr$
Depleted mantle	38	-0.25	22	0.700
Magnesite[1]	47.6	-1.9	3.17	0.710
Magnesite[2]	47.6	-1.9	3.53	0.720
Dolomite[1]	22	-1.89	1311	0.7099
Dolomite[2]	22	-3	1800	0.7036

Note:

The MgO and δ^{26}Mg of depleted mantle are from Ke et al. (ref. [46]), Teng et al. (ref. [20]); The MgO of magnesite and dolomite are from Li et al., (ref. [47]). The δ^{26}Mg of magnesite[1] and magnesite[2] are from Li et al. (ref. [47]); The δ^{26}Mg of dolomite[1] are from Huang and Xiao, (ref. [48]), Li et al., (ref. [49]); The δ^{26}Mg of dolomite[2] is from Wang et al. (ref. [50])

The Sr content of depleted mantle is from Palme and O'Neill, (ref. [51]), $^{87}Sr/^{86}Sr$ is from Zhang et al. (ref. [52]), were corrected by 2.55 Ga; The Sr and $^{87}Sr/^{86}Sr$ of magnesite[1] and magnesite[2] are from Gorokhov et al. (ref. [53]); The Sr and $^{87}Sr/^{86}Sr$ of dolomite[1] are from Huang and Xiao, (ref. [48]), Li et al., (ref. [49]); The Sr of dolomite[2] is from Wawrzenitz et al. (ref. [54]) and $^{87}Sr/^{86}Sr$ of dolomite[2] is from Romer et al. (ref. [55]) .

References

1. Zhao, G. C., Sun, M., Wilde, S. A. & Li, S. Z. Late Archean to Paleoproterozoic evolution of the North China Craton: key issues revisited. *Precambrian Res.* **136(2),** 177-202 (2005).

2. Jian, P., Kröner, A., Windley, B. F., Zhang, Q., Zhang, W. & Zhang, L.Q. Episodic mantle melting-crustal reworking in the late Neoarchean of the northwestern North China Craton: Zircon ages of magmatic and metamorphic rocks from the Yinshan Block. *Precambrian Res.* **222-223,** 230-254 (2012).

3. Ma, X. D., Guo, J. H., Liu, F., Qian, Q. & Fan, H. R. Zircon U–Pb ages, trace elements and Nd–Hf isotopic geochemistry of Guyang sanukitoids and related rocks: Implications for the Archean crustal evolution of the Yinshan Block, North China Craton. *Precambrian Res.* **230,** 61-78 (2013).

4. Zhang, X., Yuan, L., Xue, F. & Zhai, M. Neoarchean metagabbro and charnockite in the Yinshan block, western North China Craton: Petrogenesis and tectonic implications. *Precambrian Res.* **255,** 563-582 (2014).

5. Wang, D., Guo, J., Huang, G. & Scheltens, M. The Neoarchean ultramafic–mafic complex in the Yinshan Block, North China Craton: Magmatic monitor of development of Archean lithospheric mantle. *Precambrian Res.* **270,** 80-99 (2015).

6. Wang, D. & Guo, J. Late Archean high-pressure pelitic granulites in the Yinshan Block, North China Craton. *Precambrian Res.* **303,** 251-267 (2017).

7. Wang, X. et al. Petrogenesis and tectonic setting of Neoarchean tonalitic-trondhjemitic-granodioritic gneisses in the Xiwulanbulang area of the Yinshan block, North China craton. *GSA Bulletin*. **135(11-12),** 2922-2938 (2023).

8. Sun, S. S. & McDonough, W. F. Chemical and isotopic systematics of oceanic basalts:Implications for mantle composition and processes. J. Geol. Soc. London. Special Publications. **42(1),** 313-345 (1989).

9. Polat, A., Appel, P. W. U. & Fryer, B. J. An overview of the geochemistry of Eoarchean to Mesoarchean ultramafic to mafic volcanic rocks, SW Greenland: Implications for mantle depletion

and petrogenetic processes at subduction zones in the early Earth. *Gondwana Res.* **20(2),** 255-283 (2011).

10. Taylor, S. R. & McLennan, S. M. The geochemical evolution of the continental crust. *Rev. Geophys*. **33(2),** 241-265 (1995).
11. Rudnick, R. L. & Gao, S. Composition of the Continental Crust. Treatise Geochem 3:1-64. Composition of the Continental Crust. *Treatise Geochem.* **3,** 1-64 (2003).
12. Hofmann, A. W. Chemical differentiation of the Earth: the relationship between mantle, continental crust, and oceanic crust. *Earth Planet. Sci. Lett.* **90(3),** 297-314 (1988).
13. Tomascak, P. B., Langmuir, C. H., le Roux, P. J. & Shirey, S. B. Lithium isotopes in global mid-ocean ridge basalts. *Geochim. Cosmochim. Acta.* **72(6),** 1626-1637 (2008).
14. Tan, D. -B., Xiao, Y., Dai, L. -Q., Sun, H., Wang, Y. & Gu, H. -O. Differentiation between carbonate and silicate metasomatism based on lithium isotopic compositions of alkali basalts. *Geology.* **50(10),** 1150-1155 (2022).
15. Teng, F. -Z., Wadhwa, M. & Helz, R. T. Investigation of magnesium isotope fractionation during basalt differentiation: Implications for a chondritic composition of the terrestrial mantle. *Earth Planet. Sci. Lett.* **261(1),** 84-92 (2007).
16. Wang, X. -J. et al. Magnesium isotopic fractionation during basalt differentiation as recorded by evolved magmas. *Earth Planet. Sci. Lett.* **565,** 116954 (2021).
17. Zhong, Y., Chen, L. -H., Wang, X. -J., Zhang, G. -L., Xie, L. -W. & Zeng, G. Magnesium isotopic variation of oceanic island basalts generated by partial melting and crustal recycling. *Earth Planet. Sci. Lett.* **463,** 127-135 (2017).
18. Xiong, S., Wang, F., Wang, Y. -N., Hong, K. -C., Zhang, S. -W., Liu, S. -A. & Xu, W. -L. Three-dimensional variations in carbon inputs to a subduction zone based on Mg–Zn isotopes. *Geochim. Cosmochim. Acta* (2025).
19. Schiano, P., Monzier, M., Eissen, J. P., Martin, H. & Koga, K. T. Simple mixing as the major control of the evolution of volcanic suites in the Ecuadorian Andes. *Contrib. Mineral Petrol.* **160(2),** 297-

312 (2010).

20. Teng, F. -Z., Li, W. -Y., Ke, S., Marty, B., Dauphas, N., Huang, S., Wu, F. -Y. & Pourmand, A. Magnesium isotopic composition of the Earth and chondrites. *Geochim. Cosmochim. Acta.* **74(14),** 4150-4166 (2010).

21. Zafar, T. et al. Petrogenesis, platinum-group element geochemistry and geodynamic evolution of the Cretaceous Chilas gabbros, Kohistan island arc, NE Pakistan. *Lithos.* **372-373,** 105691 (2020).

22. Herzberg, C. Petrology and thermal structure of the Hawaiian plume from Mauna Kea volcano. *Nature.* **444,** 605–609 (2006).

23. Sobolev, A. V. et al. The amount of recycled crust in sources of mantle-derived melts. *Science.* **316,** 412–417 (2007).

24. Kessel, R., Schmidt, M., Ulmer, P. & Pettke, T. Trace element signature of subduction-zone fluids, melts and supercritical liquids at 120–180 km depth. *Nature.* **437,** 724–727 (2005).

25. Liu S. C., Xia, Q. K., Choi, S. H., Deloule, E., Li, P. & Liu, J. Continuous supply of recycled Pacific oceanic materials in the source of Cenozoic basalts in SE China: the Zhejiang case. *Contrib. Mineral Petrol.* **171,** 100 (2016).

26. Stracke, A., Bizimis, M. & Salters, V. J. M. Recycling oceanic crust: Quantitative constraints, *Geochem. Geophys. Geosyst.* **4,** 8003 (2003).

27. Staudigel, H., Plank, T., White, B. & Schmincke, H. Geochemical fluxes during seafloor alteration of the basaltic upper oceanic crust: DSDP Sites 417 and 418. In Subduction: Top to Bottom (eds G. E. Bebout, D. W. Scholl, S. H. Kirby and J. P. Platt). *Geophys. Monogr. Ser.* **96,** 19–38 (1996).

28. Kelley, K. A., Plank, T., Farr, L., Ludden, J. & Staudigel, H. Subduction cycling of U, Th, and Pb. *Earth Planet. Sci. Lett.* **234,** 369–383 (2005).

29. Zhang, S. W., Wang, F., Xing, K. C., Wang, Y. N., Xu, W. L. & Yang, D. B. A stagnant subducted slab accelerates the deep Earth carbon cycle. *Geology*. **53 (9),** 769–774 (2025).

30. Plank, T. & Manning, C. E. Subducting carbon. *Nature.* **574,** 343–352 (2019).

31. Farsang, S. et al. Deep carbon cycle constrained by carbonate solubility. *Nat. Commun.* **12 (1),** 1–9

(2021).

32. Arzilli, F., Burton, M., La Spina, G., Macpherson, C. G., van Keken, P. E. & McCann, J. Decarbonation of subducting carbonate-bearing sediments and basalts of altered oceanic crust: Insights into recycling of CO_2 through volcanicarcs. *Earth Planet. Sci. Lett.* **602,** 117945 (2023).

33. Zeng, G., Chen, L. H., Hofmann, A. W., Wang, X. J., Liu, J. Q., Yu, X. & Xie, L. W. Nephelinites in eastern China originating from the mantle transition zone. *Chem. Geol.* **576,** 120276 (2021).

34. Pearce, J. A. & Peate, D. W. Tectonic Implications of the Composition of Volcanic Arc Magmas. *Annu Rev Earth Pl Sc*. **23,** 251-285 (1995).

35. Russell, W. A., Papanastassiou, D. A. & Tombrello, T. A. Ca isotope fractionation on the earth and other solar system materials. *Geochim. Cosmochim. Acta.* **42,** 1075–1090 (1978).

36. Lin, J., Liu, Y. S., Yang, Y. H. & Hu, Z. C. Calibration and correction of LA–ICP–MS and LA–MC–ICP–MS analyses for element contents and isotopic ratios. *Solid Earth Sciences*. **1,** 5–27 (2016).

37. Zhang, W., Hu, Z. C. & Liu, Y. S. Iso–Compass: new freeware software for isotopic data reduction of LA–MC–ICP–MS. *J Anal Atom Spectrom.* **35,** 1087–1096 (2020).

38. Lin, J., Liu, Y. S., Hu, Z. C., Chen, W., Zhang, L. & Chen, H. H. Accurate measurement of Lithium isotopes in eleven carbonate reference materials by MC–ICP–MS with soft extraction mode and 10^{12} Ω resistor high-gain faraday amplifiers. *Geostand Geoanal Res*. **43,** 277–289 (2019).

39. Wang, Y. Zhang, Y. C., Li, X., Ke, S., Sun, A. Y., Yang, R. Y., Yang, W. J. & He, Y. S. Purification of Mg from extremely low-Mg felsic rocks for isotopic ratio determination by MC–ICP–MS. *J Anal Atom Spectrom.* **37,** 497–507 (2022).

40. Bao, Z. A., Huang, K. J., Huang, T. Z., Shen, B., Zong, C. L., Chen, K. Y. & Yuan, H. L. Precise magnesium isotope analyses of high-K and low-Mg rocks by MC–ICP–MS. *J Anal Atom Spectrom.* **34,** 940–953 (2019).

41. Wang, J., Tappe, S., Wang, Q., Li, J., Zou, Z. Q. & Tang, G. J. Carbon cycling during the India-Asia collision revealed by $\delta^{26}Mg$–$\delta^{66}Zn$–$\delta^{98}Mo$ evidence from ultrapotassic volcanoes in NW Tibet. *Geology.* **52,** 672–677 (2024).

42. Wan, Y. S. et al. Spatial and temporal distribution，compositional characteristics and formation and evolution of Archean TTG rocks in the North China Craton: A synthesis. *Acta Petrol. Sin.* **33(05),** 1405-1419 (2017).

43. Pearce, J. A. A User's Guide to Basalt Discrimination Diagrams. In: Wyman, D.A., Ed., Trace Element Geochemistry of Volcanic Rocks: Applications for Massive Sulphide Exploration, Geological Association of Canada, *Short Course Notes.* **12,** 79-113 (1996).

44. Rickwood, P. C. Boundary lines within petrologic diagrams which use oxides of major and minor elements. *Lithos.* **22(4),** 247-263 (1989).

45. Boynton, W. V. Chapter 3 - Cosmochemistry of the Rare Earth Elements: Meteorite Studies. In: P. Henderson (Editor), Developments in Geochemistry. Elsevier, pp. 63-114 (1984).

46. Ke, S, Teng, F. Z., Li, S. G., Gao, T., Liu, S. A., He, Y. & Mo, X. Mg, Sr, and O isotope geochemistry of syenites from northwest Xinjiang, China: Tracing carbonate recycling during Tethyan oceanic subduction. *Chem Geol.* **437,** 109–119 (2016).

47. Li, S. G. & Wang, Y. Formation time of the big mantle wedge beneath eastern China and a new lithospheric thinning mechanism of the North China Craton—Geodynamic effects of deep recycled carbon. *Sci. China Earth Sci.* **61,** 853–868 (2018).

48. Huang, J. & Xiao, Y. L. Mg-Sr isotopes of low-δ26Mg basalts tracing recycled carbonate species: Implication for the initial melting depth of the carbonated mantle in Eastern China. *Int Geol Rev.* **58,** 1350–1362 (2016).

49. Li, S. G. et al. Deep carbon cycles constrained by a large-scale mantle Mg isotope anomaly in eastern China. *Natl Sci Rev.* **4,** 111–120 (2017).

50. Wang, S. -J., Teng, F. -Z. & Li, S. -G. Tracing carbonate-silicate interaction during subduction usinf magnesium and oxygen isotopes. *Nature Comm.* **5,** 5328 (2014).

51. Palme, H. & O'Neill, H. Cosmochemical Estimates of Mantle Composition. in The Mantle and Core. vol. 3, Elsevier, pp. 1-39 (2013).

52. Zhang, H. F., Goldstein, S. L., Zhou, X. H., Sun, M., Zheng, J. P. & Cai, Y. Evolution of

subcontinental lithospheric mantle beneath eastern China: Re–Os isotopic evidence from mantle xenoliths in Paleozoic kimberlites and Mesozoic basalts. *Contrib Mineral Petrol.* **155,** 271–293 (2008).

53. Gorokhov, I. M. et al. Isotope composition of strontium, carbon, and oxygen in magnesian carbonates of the Onot greenstone belt. Dokl. *Earth Sc.* **455,** 341–345 (2014).
54. Wawrzenitz, N., Romer, R. L., Grasemann, B. & Morales, L. G. Pre-UHP titanite archives pro- and retrograde episodes of fluid-marble-interaction (Dabie Shan UHP unit, China). *Lithos.* **350-351,** 105232 (2019).
55. Romer, R. L., Wawrzentiz, N. & Oberhänsli, R. Anomalous unradiogenic 87Sr/86Sr ratios in ultrahigh-pressuer crustal carbonates – evidence for fluid infiltration during deep subduction? *Terra Nova*. **15,** 330-336 (2003).